

(Sub-)femtosecond control of molecular reactions *via* tailoring the electric field of light

Cite this: *Phys. Chem. Chem. Phys.*, 2013, **15**, 9448

Matthias F. Kling,^{*ab} Philipp von den Hoff,^c Irina Znakovskaya^b and Regina de Vivie-Riedle^{*c}

We review recent progress in the control over chemical reactions by employing tailored electric field waveforms of intense laser pulses. The sub-cycle tailoring of such waveforms permits the control of electron dynamics in molecules on sub-femtosecond timescales. We show that laser-driven electron dynamics in molecules has the potential to control chemical reactions. In the presence of strong fields, electron and nuclear motion are coupled, requiring models beyond the Born–Oppenheimer approximation for their theoretical treatment. Various mechanisms for the lightwave control of molecular reactions are described, and their relevance for the control of diatomic molecular reactions is discussed. Rapid experimental and theoretical progress is currently being made, indicating that attosecond controlled chemistry is within reach.

Received 8th February 2013,

Accepted 8th April 2013

DOI: 10.1039/c3cp50591j

www.rsc.org/pccp

1 Introduction

Research on laser-induced physical and chemical processes allows unparalleled insight into the working of nature at the microscopic level by offering measurement techniques with unprecedented resolution and accuracy. Chemical processes are determined by nuclear motions, which occur on timescales reaching into the femtosecond ($1 \text{ fs} = 10^{-15} \text{ s}$) domain.¹

^a J.R. Macdonald Laboratory, Physics Department, Kansas State University, 116 Cardwell Hall, Manhattan, KS 66506, USA

^b Max-Planck-Institut für Quantenoptik, Hans-Kopfermann-Str. 1, 85748 Garching, Germany. E-mail: matthias.kling@mpq.mpg.de

^c Department of Chemistry, Ludwig-Maximilians-Universität München, Butenandtstr. 11, 81377 München, Germany. E-mail: Regina.de_vivie@cup.uni-muenchen.de



Matthias F. Kling

Matthias Kling was born in Hanover, Germany. He graduated in physics in 1998 at the Georg-August-University of Göttingen, Germany, and received his PhD there in 2002 in the field of physical chemistry. After post-docs at UC Berkeley in Berkeley (USA) and AMOLF in Amsterdam (The Netherlands), he joined the Max Planck Institute of Quantum Optics in Garching, Germany, as a research group leader. He holds a co-appointment as assistant

professor at the Kansas-State University, USA, since 2009. In 2013 he will join the Department of Physics at the Ludwig-Maximilians-University of Munich, Germany, as associate professor. The research of his group is focused on electron dynamics in atoms and molecules in strong laser fields and attosecond nanophysics.



Philipp von den Hoff

Philipp von den Hoff was born in Munich, Germany. He received his diploma degree in chemistry from the Ludwig-Maximilians-University of Munich in 2007 and obtained his PhD in theoretical chemistry there in 2012. Within his diploma and his PhD thesis, he performed theoretical studies on coupled electron and nuclear dynamics in small molecules and their coherent control.

The driving force for the nuclear motion is the potential, which arises from electronic motion. Electronic motion can occur on much faster, attosecond timescales ($1 \text{ as} = 10^{-18} \text{ s}$). Recent progress in controlling and tracing ultrafast electronic motion in chemical reactions was fueled by the development of strong few-cycle near-infrared (NIR) and mid-infrared (MIR) light pulses as well as their conversion to ultrashort extreme ultraviolet light pulses by high-harmonic generation (HHG). These light pulses can be used to steer and/or to probe the evolution of the electron and nuclear dynamics, which is unfolding upon their interaction with a molecule.

With the experimental realizations of such ultra-short light pulses, the challenge to steer a chemical reaction by modifying the potential energy landscape of the system arises. This can be achieved by a dynamic Stark shift,² however, a more direct method is to form and guide an electronic wavepacket inside a molecule to steer the reaction pathway. The formation of electronic wavepackets as a result of the removal of an electron (through ionization) on attosecond timescales was recently considered by Cederbaum and co-workers^{3,4} and by Remacle and Levine.⁵ Since the electronic structure that results from the removal of one of the electrons (*e.g.* from the highest-occupied molecular orbital (HOMO)) of a neutral molecule will generally differ from the ground state of the cation that is formed upon ionization, an ultrafast removal of an electron will form a coherent superposition of various electronic states. Comparing a wide range of electronic systems, Breidbach and Cederbaum observed that the sudden removal of an electron is accompanied by a characteristic time response that is completed in about 50 as.³ This time response is interpreted in terms of a filling—upon ionization—of the exchange–correlation hole that is associated with the ionized electron, by its neighboring electrons. Remacle and Levine argued that sudden ionization of a molecule may lead to electron transport across the ionic structure that is formed and occurs in less than one femtosecond.⁵ These timescales are much too fast for the nuclei to

react, *i.e.* to introduce a nuclear motion. The usage of ultrashort laser pulses to strip electrons from molecules is therefore not optimal to control a chemical reaction.

An alternative route to create and guide electronic wavepackets is to superimpose preselected electronic states in a coherent way by laser radiation. A suitable superimposed state can control the timescale of the electron dynamics as well as the general form and the pathway of the wavepacket. To gain full control over electronic wavepackets, it is also required to control and steer the phase of the electronic superposition. This can be achieved by tailoring the waveform of the electric field which prepares and/or modifies the superposition state. Thus the electric field waveform of the light pulse adds a new dimension to the control of chemical reactions. By steering charges within molecules, the possibilities of controlling the outcome of light-induced chemical reactions may be significantly enhanced and can lead to the formation or even to the cleavage of chemical bonds in the sense of charge-directed reactivity.⁶

Tailoring the electric field of oscillatory waveforms on sub-cycle timescales opens the door to the control of electron dynamics in molecules on their natural timescale. The electric field of a light pulse in the few-cycle domain may be described as $\varepsilon(t) = E_0(t) \cos(\omega t + \phi)$, with envelope $E_0(t)$, carrier frequency ω and the phase between the carrier wave and the envelope (carrier envelope phase; CEP) ϕ . Examples of few-cycle pulses with different CEP values are shown in Fig. 1. To utilize the CEP as a control parameter, the electric field waveform of a few-cycle laser pulse can be either stabilized⁷ or precisely measured for each laser shot.^{8,9} Light that is synthesized from ultra-broadband continua (spanning over 1.5 octaves) allows to even sculpt the electric field waveforms with sub-cycle precision.¹⁰ Such a synthesized field promises a significant advance in the control of electron and molecular reaction dynamics. In this article, we will review and discuss recent experimental and theoretical progress on the light waveform control of electron



Irina Znakovskaya

Irina Znakovskaya was born in Kharkov, Ukraine. She received her diploma degree in chemistry from the Novosibirsk State University in 2006, worked as a research fellow at the University of Basel until 2007 and obtained her PhD in physics at the Ludwig-Maximilians-University in 2012. During her PhD, she studied the directional control of strongly-coupled electron and nuclear dynamics in molecules in intense, femtosecond laser fields.



Regina de Vivie-Riedle

Regina de Vivie-Riedle was born in Wuppertal, Germany. She graduated in chemistry from the Friedrich-Wilhelm-University of Bonn, Germany, in 1987. In 1997, she did the Habilitation in theoretical chemistry at the Freie University Berlin. She did two postdocs, one at the Max Planck Institute of Quantum Optics (MPQ) in Garching and one at the Joint Institute for Laboratory Astrophysics (JILA) in Boulder. From 1997 to 2002 she was a

C3 professor at the MPQ. Since 2003, she has been the leader of the theoretical femtosience group at the Ludwig-Maximilians-University in Munich. Her research topics include ultrafast photoinduced molecular dynamics and coherent control theory.

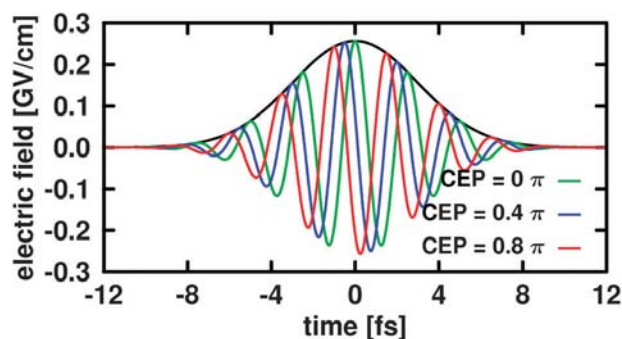


Fig. 1 Carrier-envelope phase (CEP) control of few-cycle pulses. The electric field for different CEP values is shown in color. The pulse envelope is indicated by a solid black line.

motion in molecules and show perspectives for the future of sub-cycle coherent control of molecular reaction dynamics.

The article is organized as follows: first we give a brief introduction into experimental techniques for the light-waveform control of chemical reactions (Section 2) and into a theoretical approach, which can be used to interpret such data (Section 3). Subsequently, we review the experiments and theoretical results, where CEP-stabilized, few-cycle pulses have been used to control electron localization in the dissociative ionization of diatomic molecules (Sections 4.1 and 4.2). We then theoretically introduce a control scheme utilizing CEP-stabilized light pulses to precisely steer photochemical reactions which proceed through conical intersections (CoIn) and conclude the article with an outlook.

2 Experimental techniques

2.1 Generation of few-cycle laser pulses with stable electric field waveform

We will briefly introduce the two types of laser sources used in the experiments on the lightwave control of molecular reactions discussed here: (1) few-cycle near-infrared (NIR) pulses with stabilized^{11,12} or tagged CEP^{13,14} derived from amplified Ti:sapphire laser systems and (2) few-cycle mid-infrared (MIR) pulses with passively stabilized CEP derived from an optical parametric amplifier (OPA)–optical parametric chirped pulse amplifier (OPCPA) laser system.¹⁵

Transform-limited, phase-stable laser pulses in the NIR (20 fs pulses at 800 nm central wavelength with energies in the mJ to tens of mJ range) can be generated at kHz repetition rates from commercial, amplified Ti:sapphire laser systems.^{16,17} These pulses can be spectrally broadened with gas-filled hollow-core fibers and compressed with chirped-mirrors to pulse durations of below 4 fs.¹¹ The duration of these pulses may be monitored using commercial dispersion-balanced autocorrelators or frequency-resolved optical gating devices.^{18,19} Currently, the most precise way to determine the sub-cycle evolution of the electric field of a few-cycle pulse is to perform an attosecond streaking experiment.^{20,21} This method is particularly powerful for synthesized waveforms.¹⁰

CEP-stabilization can be realized by active feedback loops.^{22–25} The overall CEP jitter for a kHz amplifier system can be reduced to less than 100 mrad over a period of several hours.^{8,11} The novel feed-forward CEP-stabilization approach^{26,27} is currently being implemented into amplified Ti:sapphire laser systems and will likely make it easier to perform CEP-dependent measurements in the near future. In experiments that aim to record a molecular process as a function of the CEP, phase-stabilized pulses can be employed, where the CEP is varied by insertion of dispersive material (*e.g.* with a pair of wedged fused silica plates) into the beam path. The recent implementation of phase-tagging^{9,13,14} opens another route to the measurement of CEP-dependent processes: the fragments from a molecular process and the CEP are measured for each individual laser shot. The CEP does not need to be stabilized and is left random, so that all pulse parameters besides the CEP stay exactly the same and measurements can be conducted over a longer time period and with better averaging over laser parameter fluctuations than is possible with CEP-stabilized pulses.²⁸ While CEP-tagging is becoming the standard approach for CEP-dependent measurements,^{28–30} there are cases where the CEP still needs to be stable, such as the generation of isolated attosecond pulses for tracing the electric field waveform and for probing ultrafast molecular dynamics.³¹ Furthermore, ultra-broadband waveform synthesis requires laser pulses with stable and controlled CEP.^{10,32}

Passively-CEP-stable, few-cycle pulses in the MIR can be derived from OPAs. Here, difference frequency mixing is employed for generating the MIR seed, resulting in a signal that is passively CEP-stabilized without the need for an active feedback loop.^{15,33} As shown in ref. 34 this stabilization scheme significantly simplifies CEP-dependent measurements, allowing for longer continuous data acquisition. In the laser system described in ref. 15 and used for the studies described in this article, the generated phase-stable seed (center wavelength of 2.1 μm) was amplified in three OPCA stages pumped by a synchronized, picosecond Nd:YLF laser. The output of the OPCA system was compressed to 16–25 fs by propagating the pulses through a 10 cm-long silicon rod. The resulting output pulses can be characterized using frequency-resolved optical gating. This laser system delivered few-cycle MIR pulses at a kHz repetition rate with a few hundreds of μJ per pulse. The CEP was varied by the insertion of dispersive material into the beam path.

2.2 Imaging of fragments from molecular reactions

Imaging techniques such as velocity-map imaging (VMI)³⁵ or reaction microscopy (REMI),³⁶ which provide the full momentum distributions of charged particles, have been successfully employed in recent studies on the lightwave control of electron dynamics in atoms,^{13,37–39} molecules,^{40–48} and nanostructures.⁴⁹ While both REMI and VMI are capable of measuring the momentum distributions of charged fragments, they have individual advantages and disadvantages. REMI allows the detection of particles in coincidence providing more insight into the reaction mechanisms and pathways. The number of

hits per laser shot, however, that can be recorded using the microchannel plate (MCP)/delay line detectors is limited (up to a few hits on the ion and the electron detector). These restrictions result in count rates of a few per laser shot (or less than one if coincidence detection is used). In VMI, the density of the gas target is mostly limited by the occurrence of space charge effects and eventually by the need to maintain sufficiently low pressures to operate the MCP detector. The number of hits onto the detector per laser shot can be many orders of magnitude higher than for a REMI. Generally, if coincident detection of multiple charged particles is advantageous, the use of a REMI is desirable. If coincident detection is not needed, VMI is a good choice as it allows for much higher count rates and thus shorter acquisition times and better statistics. Due to this advantage and systems with only limited complexity that have been studied so far, a larger number of experiments on the lightwave control of molecular dynamics have been conducted with VMI being also reflected in this article. Recent progress, however, in CEP-tagging allows for longer data acquisition times and thus a better implementation of CEP-dependent studies employing REMI. It is foreseeable that this recent technological advance together with the wider use of self-phase-stabilized laser systems will promote REMI studies.

Being more important for the research contained in this article, VMI experiments are described in more detail in the following. Few-cycle NIR or MIR pulses are focused using a spherical mirror into the VMI spectrometer,^{35,50} see Fig. 2. The electron/ion optics of a standard VMI spectrometer consist of repeller, extractor, and ground plates, where a static field is used to project electrons or ions resulting from the interaction of a molecule with a strong laser pulse. An MCP/phosphor

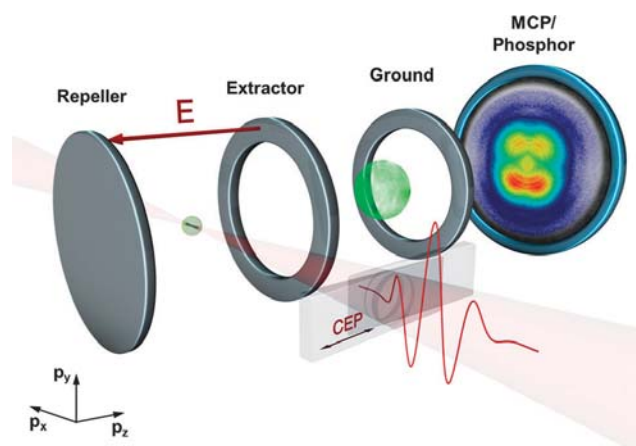


Fig. 2 Setup for the measurement of molecular dissociation with ultrashort intense laser pulses: the waveform of the laser pulses is controlled with a pair of glass wedges. The laser pulses interact with the molecules in a velocity map imaging (VMI) spectrometer, in which the resulting distribution of ions (here C^+ fragments from dissociative ionization of CO) after the break-up of the molecules is imaged onto a detector (MCP/phosphor screen assembly). The image on the detector displays an up-down asymmetry along the vertical polarization axis of the laser that was measured for a certain CEP value. Figure courtesy: Christian Hackenberger, MPQ.

screen assembly in combination with a camera recording light flashes on the phosphor screen is used for the 2-dimensional detection. In the case of single-shot phase-tagged studies, an ultrafast camera which permits the recording of a high number of events per laser shot is required.¹⁴ Different ionic species can be distinguished by their time-of-flight (TOF) and appropriate gating of the MCP with a laser-triggered, fast high-voltage-switch.

The peak intensity of the few-cycle pulses in the focus (typically in the range of 10^{13} to 10^{15} W cm⁻² for the studies described here) can be determined from the cutoff in electron spectra recorded for the above-threshold ionization (ATI) of Xe^{37,51} under the same experimental conditions as for the molecular experiments.

In the case of cylindrical symmetry of the electron or ion emission, 3D momentum distributions may be obtained from the 2D projections by Abel inversion, *e.g.* by implementing an iterative inversion procedure.⁵² In our notation of the axes we will follow the work by Vrakking.⁵² The measured ion and electron distributions lie in the x - y plane with symmetry following the laser polarization which is parallel to the y -axis. The polar angle θ is defined as the angle between a vector \vec{p} in the detector plane and the y -axis. The z -axis is the projection coordinate along the spectrometer axis.

3 Coupled electron- and nuclear-dynamics

The key aspect in the following reactions is to control the dynamics of the nuclei by the preparation and the guidance of an electronic wavepacket. To describe these processes theoretically it is imperative to treat the nuclear and electron dynamics in a coupled manner; however, a theoretical description of electron dynamics in multi-electron molecules (with at least more than one nucleus) is a challenge, and its appropriate treatment is the aim of state-of-the-art research. Most approaches use time-dependent analogs of well-established quantum chemical methods. Based upon the time-dependent Hartree–Fock theory⁵³ and the (explicitly) time-dependent density-functional theory⁵⁴ there are many expansions to incorporate electron correlation and make use of post-Hartree–Fock methods like time-dependent-configuration-interaction (TD-CI),^{55,56} time-dependent multi-configuration-self-consistent-field (TD-MCSCF)⁵⁷ and multi-configuration time-dependent-Hartree–Fock (MC-TDHF).⁵⁸ In other approaches the electronic wavefunction is directly propagated using Green’s function formalism⁵⁹ or on the basis of molecular orbitals.⁵

To describe reactions where the nuclear coordinates change by definition, an approach which describes both electron and nuclear dynamics equally is needed. In addition it is necessary to synchronize the timescale of the electrons with the timescale of the moving nuclei. For the three-body-system D_2^+ the coupled dynamics can be fully calculated quantum mechanically.^{60,61} Moreover, a multi-configuration electron-nuclear dynamics method⁶² exists, which may handle more than two nuclei and one electron. While these methods describe the electronic and nuclear motion very accurately,

the calculations are computationally demanding and not yet realizable for larger molecular systems. The group of Takatsuka⁶³ therefore introduced an ansatz to couple electron dynamics in the eigenstate system to classical nuclear motion. But here the quantum nature of the nuclei is completely neglected.

To calculate the coupled nuclear- and electron-dynamics, even for larger quantum systems, we used a recently developed viable ansatz⁶⁴ which is capable of treating larger molecules. This approach includes electronic structure calculations as well as nuclear quantum dynamics and thus takes the quantum nature of both the nuclei and the electrons into account. The fundamental steps of this method are outlined below.

3.1 Nuclear quantum dynamics using the Born–Oppenheimer approximation

The initial step to calculate the coupled nuclear- and electron-dynamics following the approach in ref. 64 is to identify the different electronic states involved in the reaction and in the formation of the electronic wavepacket. Upon this selection, the nuclear quantum dynamic calculations are carried out. During the laser interaction, the individual electronic states are coupled. This coupling is described within the semi-classical dipole approximation by $-\mu_{ij}\varepsilon(t)$. Here,

$$\mu_{ij} = \int \psi_i^*(r; R) \hat{\mu} \psi_j(r; R) dr \quad (1)$$

is the transition dipole moment between the electronic states i and j and $\varepsilon(t)$ the time-dependent electric field. In the framework of the applied Schrödinger picture, μ_{ij} is calculated using the time-independent electronic wavefunctions $\psi_i(r; R)$, while the time evolution is kept in the nuclear wavefunction propagating on the corresponding electronic states. Thus the only time-dependence in the Hamilton operator arises from the light field $\varepsilon(t)$:

$$\hat{H}_{\text{nuc}} = \begin{pmatrix} \hat{T}_{\text{nuc}} & 0 & \cdots \\ 0 & \hat{T}_{\text{nuc}} & \cdots \\ \vdots & \vdots & \ddots \end{pmatrix} + \begin{pmatrix} \hat{V}_1 & -\mu_{12}\varepsilon(t) & \cdots \\ -\mu_{12}\varepsilon(t) & \hat{V}_2 & \cdots \\ \vdots & \vdots & \ddots \end{pmatrix}. \quad (2)$$

Here, T_{nuc} is the kinetic Hamiltonian for the nuclei and V_i are the preselected electronic surfaces. The total nuclear wavefunction $\chi_{\text{tot}}(t)$ of the system is a column vector:

$$\chi_{\text{tot}}(t) = \begin{pmatrix} a_1(t)\chi_1(t) \\ a_2(t)\chi_2(t) \\ \vdots \end{pmatrix}. \quad (3)$$

The individual rows are composed of the coefficients a_i and the basis function χ_i of each individual electronic state. Using

the Hamiltonian eqn (2) and the wavefunction eqn (3), the time-dependent Schrödinger-equation for the nuclei

$$i\frac{\partial}{\partial t} \begin{pmatrix} a_1(t)\chi_1(t) \\ a_2(t)\chi_2(t) \\ \vdots \end{pmatrix} = \begin{pmatrix} \hat{T}_{\text{nuc}} + \hat{V}_1 & -\mu_{12}\varepsilon(t) & \cdots \\ -\mu_{12}\varepsilon(t) & \hat{T}_{\text{nuc}} + \hat{V}_2 & \cdots \\ \vdots & \vdots & \ddots \end{pmatrix} \begin{pmatrix} a_1(t)\chi_1(t) \\ a_2(t)\chi_2(t) \\ \vdots \end{pmatrix} \quad (4)$$

can be solved by using common propagator schemes. A comparison between various propagator techniques is given in ref. 65.

3.2 Calculating the electron-dynamics within the Born–Oppenheimer approximation

To investigate the following experiments theoretically, we have to calculate the time-dependent electronic wavefunction, which constitutes the time-dependent electron density. Therefore we multiply the total wavefunction of the system

$$\Psi_{\text{tot}}(r, R, t) = \begin{pmatrix} a_1(t)\chi_1(R, t)\psi_1(r, t; R) \\ a_2(t)\chi_2(R, t)\psi_2(r, t; R) \\ \vdots \end{pmatrix}, \quad (5)$$

in analogy to the Born–Oppenheimer (BO) approximation, from left with the complex conjugate of the total nuclear wavefunction $\chi_{\text{tot}}(t)$ and subsequently integrate over the nuclear coordinates R :

$$\varphi_{\text{tot}}(r, t; R(t)) = \int \chi_{\text{tot}}^*(R, t) \Psi_{\text{tot}}(r, R, t) dR = \begin{pmatrix} \varphi_1(r, t; R(t)) \\ \varphi_2(r, t; R(t)) \\ \vdots \\ \varphi_n(r, t; R(t)) \end{pmatrix}. \quad (6)$$

The resulting coupled electronic wavefunctions $\varphi_i(r, t; R(t))$ are given by:

$$\begin{aligned} \varphi_i(r, t; R(t)) &= a_i(t)^2 \psi_i(r, t; R(t)) \\ &+ \sum_{j \neq i} a_i(t)^* a_j(t) \langle \chi_i(R, t) | \chi_j(R, t) \rangle_R \psi_j(r, t; R(t)), \end{aligned} \quad (7)$$

with $a_i(t)^2$ the population of the state i and $a_i(t)^* a_j(t) \langle \chi_i(R, t) | \chi_j(R, t) \rangle_R$ the overlap between the nuclear wavefunctions of the i and j potential energy surfaces. $\psi_i(r, t; R(t))$ denotes the electronic wavefunction of state i , which parametrically depends on the nuclear coordinates R . The Hamilton-operator for the electron dynamics on the basis of the electronic eigenstates is diagonal because the time-dependent electric field is already included in the nuclear quantum dynamics (see eqn (4)) where it steers the population transfer between the selected electronic states. Now the time-dependent electronic density $\rho_{\text{tot}}(r_1, t; R(t))$ is calculated as a function of the electron coordinate r_1 . This is done by integrating the absolute value square of the total wavefunction

over the nuclear coordinates and over the $N - 1$ electronic coordinates:

$$\begin{aligned} \rho_{\text{tot}}(r_1, t; R(t)) &= \int \Psi_{\text{tot}}^* \Psi_{\text{tot}} dR dr_2 \dots dr_N \\ &= \sum_i a_i(t)^2 \int \psi_i^*(r, t; R(t)) \psi_i(r, t; R(t)) dr_2 \dots dr_N \\ &\quad + \sum_i \sum_{j>i} 2\text{Re} \left\{ a_i(t)^* a_j(t) \langle \chi_i(R, t) | \chi_j(R, t) \rangle_R \right. \\ &\quad \left. \times \int \psi_i^*(r, t; R(t)) \psi_j(r, t; R(t)) dr_2 \dots dr_N \right\} \quad (8) \\ &= \sum_i a_i(t)^2 \int \psi_{i,0}^*(r; R(t)) \psi_{i,0}(r; R(t)) dr_2 \dots dr_N \\ &\quad + \sum_i \sum_{j>i} 2\text{Re} \left\{ a_i(t)^* a_j(t) \langle \chi_i(R, t) | \chi_j(R, t) \rangle_R \right. \\ &\quad \left. \times \int \psi_{i,0}^*(r; R(t)) \psi_{j,0}(r; R(t)) dr_2 \dots dr_N e^{-i\theta_{ij}(t)} \right\}. \end{aligned}$$

To solve the above equation, the populations $a_i(t)^2$, the overlap between the nuclear wavefunctions $a_i(t)^* a_j(t) \langle \chi_i(R, t) | \chi_j(R, t) \rangle_R$ and the time-dependent expectation value of the nuclear coordinates $R(t) = \langle \chi_{\text{tot}}(R, t) | R | \chi_{\text{tot}}(R, t) \rangle$ are evaluated using the solution of eqn (4). Subsequently, quantum chemical calculations are performed at the nuclear geometries $R(t)$ to obtain the electronic wavefunctions $\psi_{i,0}(r; R(t))$. Depending on the approach for the electronic wavefunction used by the chosen quantum chemical method the integrals $\int \psi_{i,0}^*(r; R(t)) \psi_{i,0}(r; R(t)) dr_2 \dots dr_N$ and $\int \psi_{i,0}^*(r; R(t)) \psi_{j,0}(r; R(t)) dr_2 \dots dr_N$ can be solved numerically.

The oscillation period of the electronic eigenfunctions in the complex plane is given by the eigenenergies $E_i(R(t))$, which are a function of the nuclear coordinates. Thus the phase of the electronic wavefunction needs to be calculated recursively by utilizing the phase of the previous time step.⁶⁴

$$\theta_{ij}(t) = \theta_{ij}(t - \Delta t') + E_{ij}(t) \Delta t' \quad \text{with: } E_{ij} = E_j - E_i. \quad (9)$$

As the evolution of the electronic phase is much faster than the dynamics of the nuclei, the time step $\Delta t'$ needs to be adjusted relative to the time step Δt of the nuclear dynamics.

3.3 Nuclear quantum dynamics beyond the Born–Oppenheimer approximation

In order to design a control scheme for photochemical reactions of complex systems in the presence of conical intersections (CoIns) by guiding an electronic wavepacket, we must be able to calculate ultrafast nuclear quantum dynamics beyond the Born–Oppenheimer (BO) approximation. Therefore we used the adiabatic approach described in ref. 66.

The expansion of the total molecular wavefunction into coupled BO eigenstates leads to the following Hamiltonian for the corresponding total nuclear wavefunctions $\chi_{\text{tot}}(t)$:

$$H \chi_{\text{tot}}(t) = \begin{pmatrix} T_{\text{nuc}} + V_i & K_{ij} \\ -K_{ij} & T_{\text{nuc}} + V_j \end{pmatrix} \begin{pmatrix} a_i \chi_i \\ a_j \chi_j \end{pmatrix}. \quad (10)$$

The non-adiabatic coupling (NAC) term K_{ij} between the electronic wavefunctions $\psi_i(r; R)$ and $\psi_j(r; R)$, is usually neglected within the BO approximation, but plays a crucial role in the vicinity of CoIns. This NAC is given by (see ref. 67 for example)

$$K_{ij} = - \sum_l \frac{1}{m_l} \left(f_{ij}^{(l)} \partial_{x_l} + \frac{1}{2} g_{ij}^{(l)} \right). \quad (11)$$

Here m_l denotes the mass of the l^{th} atom and x_l the Cartesian nuclear coordinates. The first- and second-order derivative (non-adiabatic) coupling elements for the electronic wavefunctions $\psi_{i,j}(r; R)$ are given by

$$\begin{aligned} f_{ij}^{(l)} &= \langle \psi_i(r; R) | \partial_{x_l} \psi_j(r; R) \rangle \\ g_{ij}^{(l)} &= \langle \psi_i(r; R) | \partial_{x_l}^2 \psi_j(r; R) \rangle. \end{aligned} \quad (12)$$

The second derivative terms $g_{ij}^{(l)}$ of the NAC are usually much smaller than the first derivative terms and hence are usually believed to be negligible. However, their omission will lead to a non-Hermitian Hamiltonian. To avoid this artefact the non-Hermitian part must be compensated. According to ref. 66 exactly the first part of the decomposition

$$g_{ij}^{(l)} = \partial_{x_l} f_{ij}^{(l)} + h_{ij}^{(l)} \quad (13)$$

is needed for this purpose. This leads to an approximation for the non-adiabatic coupling:

$$K_{ij} \approx - \sum_l \frac{1}{m_l} \left(f_{ij}^{(l)} \partial_{x_l} + \frac{1}{2} \partial_{x_l} f_{ij}^{(l)} \right), \quad (14)$$

where only the Hermitian part $h_{ij}^{(l)} = \langle \partial_{x_l} \psi_i(r; R) | \partial_{x_l} \psi_j(r; R) \rangle$ is neglected.

Within this approach we are able to describe the non-radiative transition of a molecular system between two coupled electronic states. In addition, within this adiabatic approach, extended conical intersection seams can be handled.^{66,68} This is not possible in the diabatic description, when the quantum dynamics is described in the reduced dimensions of reactive coordinates.

4 Sub-cycle coherent control of diatomic molecules using single CEP-stable pulses

Coherent control of photochemical reactions has been achieved in recent decades by manipulating the laser frequency, phase, and polarization.⁶⁹ As pointed out in the Introduction, an exciting, novel perspective is to directly control molecular rearrangement by preparing and steering electrons inside a molecule. With these induced electron dynamics, chemical bonds may be formed or broken in the sense of charge-directed reactivity.⁶ This scheme promises to very significantly enhance the possibilities of achieving coherent control over chemical reactions by guiding the electrons. The steering of electron motion can be achieved by superimposing different electronic states with defined phase-relationship.

One method is to employ CEP-stable laser electric field waveforms. Such pulses have been used to control ionization

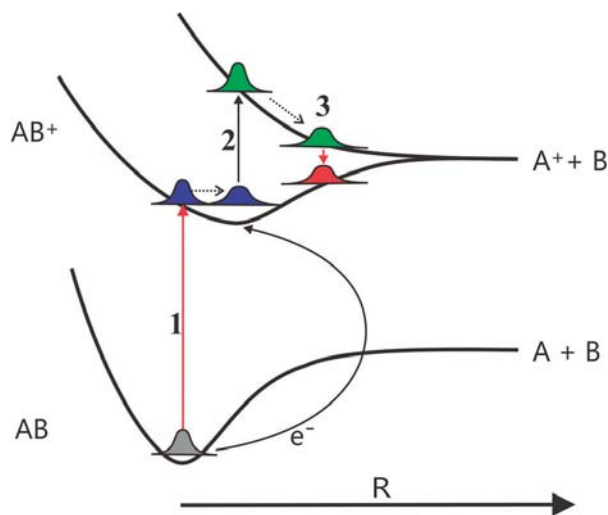


Fig. 3 Schematic illustration of the dissociative ionization of a molecule AB within three steps. Only the lowest two states of the molecular ion are shown. First step: tunnel-ionization of the neutral molecule. Second step: recollision excitation of the parent ion to dissociative electronic state(s). Third step: dissociation along the repulsive state(s) and laser-induced coupling between states of the molecular ion.

and dissociation of various diatomic molecules.^{40–46,70} We want to analyze the similarities and differences between three different experiments: (1) the dissociative ionization of D_2 (see Section 4.1), (2) CO (see Section 4.2), and additionally (3) the influence of applied laser frequency on the control of the electron localization for D_2 (see Section 4.3).

In the three experiments presented in the following sections, a single CEP-stable few-cycle pulse is used to trigger dissociative ionization and to control electron localization. The amount of electron localization is measured experimentally by monitoring the directional emission of charged fragments *via* VMI (as described in Section 2). The measured ions can originate from various reaction pathways, which can be distinguished in the VMI-spectrum due to their kinetic energy release and angular distribution. Among the different reaction pathways, the most pronounced electron localization occurs in the recollision excitation (RCE) channel. This RCE process can be broken down into three basic steps shared by all three experiments mentioned above. These processes are schematically illustrated in Fig. 3. (1) An electron originating from a high energy, occupied molecular orbital is ejected by tunnel ionization. (2) The emitted electron is driven back to the parent ion. Due to this recollision, the ion gets excited to higher lying, repulsive electronic states. (3) Along these states, the molecule dissociates, whereby the laser may induce further coupling to other states.

4.1 CEP control of electron localization in the dissociative ionization of D_2 with 760 nm pulses

Control of electron localization in the dissociation of H_2^+ and its isotopologues by means of CEP changes was theoretically predicted in ref. 60 and 71. Therefore this well-known system^{72–74} was used to demonstrate this effect in a proof of principle

experiment,⁴⁰ where the analysis was performed using different methods, including full quantum mechanical calculations.^{64,75–78}

After initial ionization, the molecules D_2 ,^{40,41,47,70} HD ⁴¹ and H_2 ^{42,45,47} only contain a single electron and the steering of this electron may be achieved by a light-induced, coherent superposition of the two electronic states $X^2\Sigma_g^+$ and $A^2\Sigma_u^+$. This CEP controlled coherent superposition localizes the electron density on one of the nuclei and thus controls the directional emission of charged and uncharged fragments upon the dissociation.

4.1.1 Experimental results of the dissociative ionization of D_2 with 760 nm pulses. The D^+ ions recorded in the VMI spectrometer were produced by linearly polarized laser pulses with durations of 5 fs at peak intensities of $I = (1.2 \pm 0.2) \times 10^{14} \text{ W cm}^{-2}$ and a center wavelength of 760 nm. Fig. 4 shows a cross-section of the three-dimensional D^+ momentum distribution in Cartesian coordinates (p_x, p_y) at $p_z = 0$, for a laser field without phase stabilization. Here, two contributions are clearly distinguishable. The first contribution ranges from 0 to $0.4 \times 10^{-22} \text{ N s}$ (0–3 eV) and the second from 0.4 to $1 \times 10^{-22} \text{ N s}$ (3–12 eV). Both fragmentation channels exhibit a maximum along the polarization axis and a minimum perpendicular to this axis. Previous studies^{79–81} suggest that D^+ ions with energies of below 3 eV originate from bond softening (BS) and enhanced ionization (EI), while the contributions above 3 eV arise from RCE and sequential ionization (SI).⁴⁰ The symmetry of the ionization pattern along the laser polarization axis (y -axis) indicates that no difference in the left *versus* right emission of D^+ ions is observed with a randomly varying phase.

With CEP stabilization, a pronounced phase dependence on the directional ion emission of the D^+ fragments is found. This is quantified by the angle-integrated asymmetry

$$A(W, \phi) = \frac{P_{\text{left}}(W, \phi) - P_{\text{right}}(W, \phi)}{P_{\text{left}}(W, \phi) + P_{\text{right}}(W, \phi)} \quad (15)$$

as a function of the fragment kinetic energy W and the laser phase ϕ . $P_{\text{left}}(W, \phi)$ and $P_{\text{right}}(W, \phi)$ are the measured ion yields in the left and right directions along the laser polarization axis. The ion yields were integrated over an angular range of 60° .

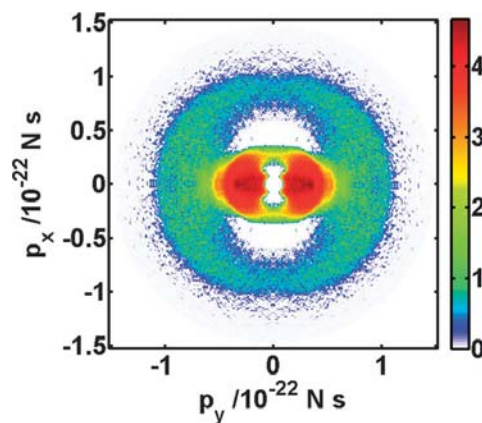


Fig. 4 Two-dimensional D^+ momentum image for D_2 dissociation in a 5 fs, $1.2 \times 10^{14} \text{ W cm}^{-2}$ laser field without phase stabilization. Reprinted from ref. 82 with copyright permission of Springer.

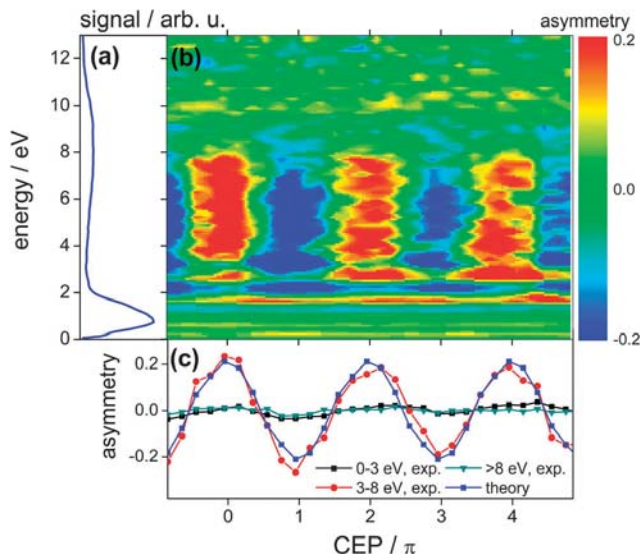


Fig. 5 (a) D⁺ kinetic energy spectrum for D₂ dissociation with 5 fs, 1.2×10^{14} W cm⁻² laser pulses without phase stabilization. (b) Map of asymmetry parameter $A(W, \phi)$ as a function of the D⁺ kinetic energy and carrier envelope phase ϕ (measured over a range of 6π with a step size of $\Delta\phi = 0.2\pi$). (c) Integrated asymmetry over several energy ranges versus carrier envelope phase ϕ and theoretical prediction. Note that the CEP is measured as a relative CEP and the offset in the CEP for the theoretical data was adjusted. Adapted from ref. 40 and 64.

We chose to analyze the ion emission within a restricted angular range because our ability to control electron motion in D₂⁺ requires that the laser couples the two lowest-lying electronic states. For molecules aligned orthogonal to the laser polarization axis, this coupling is forbidden due to optical selection rules.

Fig. 5(a) shows the angle-integrated (360°) D⁺ energy spectrum for a randomly varying CEP. Here, the two contributions between about 0–3 eV and 3–12 eV again become obvious. Panel (b) reveals that phase stabilization results in a pronounced asymmetry $A(W, \phi)$ as a function of the laser phase and the kinetic energy W of the emitted D⁺ fragments. In the region between 3 and 8 eV the asymmetry shows a sinusoidal oscillation by a variation of the CEP. This means that the directional emission of D⁺ is effectively controlled by the sub-cycle evolution of the laser field driving the dissociation. A positive [negative] asymmetry $A(W, \phi)$ represents a condition where more ionic fragments are measured on the left-hand [right-hand] side with respect to the laser polarization axis. The emission of a D⁺ ion to one side is equivalent to localization of the electron in the dissociation process on the opposite side. Thus the oscillations of asymmetry by changing ϕ demonstrate that the laser field steers the remaining electron during the dissociation. The extent of the control is further analyzed in Fig. 5(c), which displays a series of curves resulting from an integration of $A(W, \phi)$ over the energy intervals 0–3 eV and 3–8 eV. The highest degree of asymmetry with a modulation depth of 50% is observed between 3 and 8 eV. Asymmetric D⁺ ejection is observed predominantly at kinetic energies that can be assigned to the RCE channel. This in turn shows that the

electron–ion recollision is a crucial element in the mechanism leading to the observed phase control.

4.1.2 Theoretical interpretation of the dissociative ionization of D₂ with 760 nm pulses. To simulate the electron localization in the dissociative ionization of D₂ we used the theoretical approach described in Section 3. As the steering of the electrons is predominantly observed in the energy range between 3 and 8 eV (see Section 4.1.1) we exclusively follow an RCE pathway, which produces the fragments with these kinetic energies. For the dissociation and the electron localization, both following the RCE, the two electronic states X²Σ_g⁺ and A²Σ_u⁺ are needed in the quantum dynamical simulations. These potential energy surfaces together with the corresponding transition dipole moments are constructed with the help of the quantum chemistry package MOLPRO⁸³ and the Thin-Plate-Spline-algorithm.⁸⁴ First, 100 points between the internuclear distances 0.26 and 56 Å are calculated using Molpro on the CASSCF(1,2)/6-311++G** level of theory. Subsequently, these supporting points are used to generate 1200 equally spaced grid-points in the interval between 0.26 and 13.23 Å utilizing the interpolation routine. The resulting potential energy surfaces (PES) are depicted in Fig. 6.

To simulate the electron localization in the dissociation after the initial RCE, we assume ionization at the electric field maximum of the intense ultrashort laser pulse and recollision of the electron with the parent ion 1.7 fs later (corresponding to the first recollision time⁸⁶). Thereby the initially created nuclear wavepacket in the ionic ground state is excited to the A²Σ_u⁺ state and the dissociative dynamics is launched. At this point our quantum dynamical simulations start. The initial wavefunction is created by projecting the vibrational ground state wavefunction of the neutral molecule on the A²Σ_u⁺-potential. During the dissociation, the remaining laser field now couples the A²Σ_u⁺ back to the X²Σ_g⁺ (schematically shown in Fig. 6, solid gray line) and thus induces a coupled electron and nuclear motion.

For the quantum calculations, the molecules are assumed to be aligned along the laser polarization axis. The temporal evolution of the applied electric field (CEP $\phi = 0$) together with

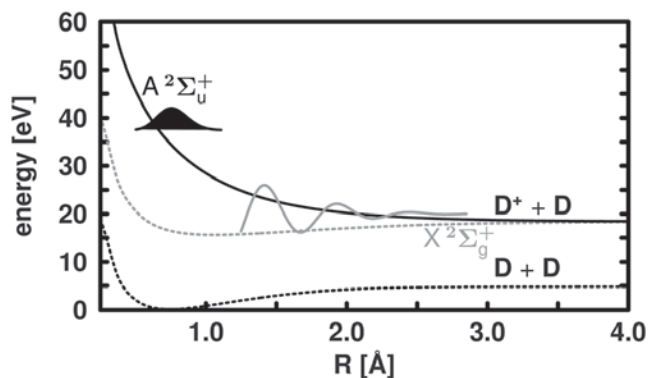


Fig. 6 Potential energy surfaces (PES) of D₂, D₂⁺ obtained by calculations described in the text. Pathway for the formation of D⁺ ions by dissociation of the molecular ion after recollision excitation. The remaining laser field (solid gray line) indicates coupling between the electronic states. Adapted from ref. 85 with copyright permission of Elsevier B.V.

the induced population dynamics during the laser interaction is drawn in Fig. 7(a) and (b). Here, the vertical black line indicates the time of recollision. In the beginning of the dissociation (1.7–5.5 fs) the superposition is built up slowly due to the laser coupling. Later during the reaction, the nuclear wavepacket reaches parts of the PES, where the energy difference between the $X^2\Sigma_g^+$ and the $A^2\Sigma_u^+$ state is resonant to the laser frequency, leading to strong molecule–light interaction with a large population exchange between 6 and 9.0 fs. The population transfer stops after about 11 fs and the final population ratio $X^2\Sigma_g^+ : A^2\Sigma_u^+$ is approximately 80 : 20. Almost the identical population dynamics is found when the CEP is flipped by π (not explicitly shown in Fig. 7(b)). The kinetic energy spectrum derived from the nuclear dynamics shows only one broad contribution between 3 and 8 eV, in good agreement with the experimentally measured fragments produced by recollision excitation.

Upon the results of the nuclear quantum dynamics, we calculated the time evolution of the electron density during the dissociation process as described in Section 3. To compare the theoretical results with the experimental ones, we consider the asymmetry in the electron density:

$$A(t) = \frac{P_{\text{left}}^{\rho}(t) - P_{\text{right}}^{\rho}(t)}{P_{\text{left}}^{\rho}(t) + P_{\text{right}}^{\rho}(t)}, \quad (16)$$

with respect to the nucleus–nucleus axis. Here, $P_{\text{left}}^{\rho}(t)$ and $P_{\text{right}}^{\rho}(t)$ denote the probabilities of finding the electron on the left and on the right D-nucleus at time t . These values can be extracted from $\rho_{\text{tot}}(r, t; R)$ by solving the integrals:

$$P_{\text{left}}^{\rho}(t) = \int_{x_{\text{min}}}^{x_{\text{max}}} dx \int_{y_{\text{min}}}^{y_{\text{max}}} dy \int_{z_{\text{min}}}^0 dz \rho_{\text{tot}}(r, t; R(t)), \quad (17)$$

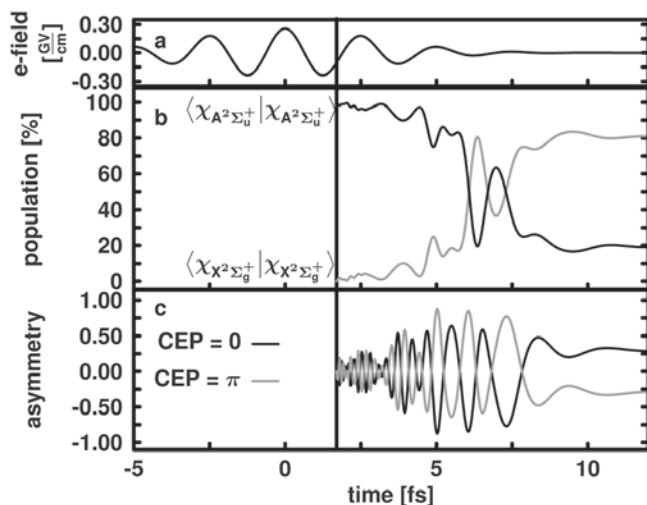


Fig. 7 Summary of the coupled electron and nuclear dynamics during the dissociation. The black vertical line indicates the time of recollision, 1.7 fs after ionization at the maximum electric field. (a) Temporal evolution of the electric field. (b) Time-dependent population of the $X^2\Sigma_g^+$ and the $A^2\Sigma_u^+$ -states of D_2^+ during the dissociation after recollision excitation (1.7 fs after ionization). (c) Temporal evolution of the asymmetry of the electronic density of D_2^+ starting from the time of recollision (black: CEP = 0; gray: CEP = π).

$$P_{\text{right}}^{\rho}(t) = \int_{x_{\text{min}}}^{x_{\text{max}}} dx \int_{y_{\text{min}}}^{y_{\text{max}}} dy \int_0^{z_{\text{max}}} dz \rho_{\text{tot}}(r, t; R(t)), \quad (18)$$

numerically on a grid. Here, the z -axis corresponds to the internuclear axis of the D_2^+ molecule and its center of mass is placed at the origin of the coordinates. Thus, asymmetry in the electron density for a given CEP ϕ at the end of the dissociation ($A(t_f)$) should be anti-correlated to the experimentally measured ion asymmetry $A(W, \phi)$ integrated over the kinetic energy range between 3 and 8 eV.

In Fig. 7(c) we visualize the temporal evolution of $A(t)$ for two CEP values (black: CEP = 0; gray: CEP = π). In the first 1.5 fs for both CEP values fast, weak oscillations in the asymmetry of the electron density can be observed. The oscillation frequency decreases during the reaction and at the same time the amplitude of $A(t)$ increases. After approximately 11 fs the temporal evolution of the asymmetry reaches its final value. Flipping the CEP by π exactly mirrors the evolution of the asymmetry (see Fig. 7(c) black and gray curves).

The overall dynamics of the asymmetry results from the interplay between the light pulse, the time evolution of the prepared superposition and the nuclear quantum dynamics. Its behavior can easily be understood from the interference term (double sum) in eqn (8). The amplitude of the asymmetry is given mainly by the overlap of the nuclear wavefunctions $a_i(t)^* a_j(t) \langle \chi_i(R, t) | \chi_j(R, t) \rangle_R$. The integral over the electronic wavefunctions ($\int \psi_{i,0}^*(r; R(t)) \psi_{j,0}(r; R(t)) dr_2 \dots dr_N$ in eqn (8)) has only minor contributions to the amplitude as the character of the electronic wavefunctions is preserved along the reaction coordinate. The oscillation frequency of the electronic wavepacket is dominated by the development of the phase term ($e^{-i\theta_{ij}(t)}$ in eqn (8)). The phase velocity is finally given by the energy difference E_{ji} between the electronic states involved. Here E_{ji} decreases during the reaction until the potential energy surfaces degenerate. This leads to a decreasing oscillation frequency. At this point the phase term remains constant and the electron dynamics end.

Flipping the CEP from 0 to π does not change the relative intensities of the electric field but switches their signs. As a result, the nuclear quantum dynamics are not affected, but the phase of the prepared electronic wavepacket inverts. This in turn causes the mirrored evolution seen in the asymmetry of the electron density (see Fig. 7(c) black and gray curves). Scanning the CEP range between 0 and 2π leads to the sinusoidal behavior of the final asymmetry in the electron density $A(t_f)$ which is shown in Fig. 5(c) and exhibits good agreement with the experimental data and the theoretical treatment in ref. 40.

4.2 CEP control of electron localization in the dissociative ionization of CO

After the proof-of-principle experiments (see Section 4.1) an important question arises: is it possible to steer electrons in more complex systems? If yes – can we understand the role of the strong-field coupling of the various potential energy surfaces that follows an initial ionization/excitation which leads to the observed control?

4.2.1 Experimental results of the dissociative ionization of CO with 740 nm pulses. We employed 4 fs, linearly polarized laser pulses at 740 nm with an intensity of $0.8 \times 10^{14} \text{ W cm}^{-2}$ to dissociatively ionize CO.⁴³ Ions that were generated at the crossing point of the laser (linearly polarized along the y -axis and propagating along the x -axis) and an effusive atomic/molecular beam were recorded using a VMI spectrometer. Inversion of the recorded projections using an iterative procedure⁵² allowed reconstruction of the original 3D ion momentum distributions. Fig. 8 shows a cross section of the 3D momentum distribution in the xy -plane at $p_z = 0$ for C^+ ions using pulses without phase stabilization. The contributions are best identified as three rings, where the first ring is the broadest (from $p = 0$ to $1 \times 10^{-22} \text{ N s}$, 0.0–1.5 eV) and most intense and exhibits additional sharp lines. The other rings appear between momenta of 1.1 to $1.3 \times 10^{-22} \text{ N s}$ (2–2.8 eV) and 1.4 to $1.6 \times 10^{-22} \text{ N s}$ (3.2–3.9 eV). The dominant features show angular distributions with minima near 0° , 90° , 180° and 270° with varying modulation depths. This observed angular distribution differs from the findings reported in ref. 87 and indicates contributions not only from the highest occupied molecular orbital (HOMO) 5σ but also from the two HOMO–1 orbitals $1\pi_{x/y}$. Ionization from more than one molecular orbital (MO) arises from the manifold of energetically-close-lying valence orbitals in multi-electron molecules and has been observed in various strong field experiments.^{43,46,88–90}

Fig. 9(a) (black line) shows the kinetic energy spectrum derived from Fig. 8 by angular integration. Again, the three contributions and the structure in the low kinetic energy region (enlarged in Fig. 9(c)) observed in Fig. 8 become obvious. Comparison of the spectrum with experiments using circularly polarized (CP) light at twice the intensity as for linear polarization (LP), which suppresses the recollision excitation, reveals a distinct decrease in intensity of all three rings (see Fig. 9(a) gray line). Thus, we conclude that recollision excitation produces the observed ionic fragments under the experimental conditions used. In the dissociation of CO^+ , the $\text{C}^+ + \text{O}$ channel is energetically favored over the $\text{C} + \text{O}^+$ channel.⁴³ Thus, we

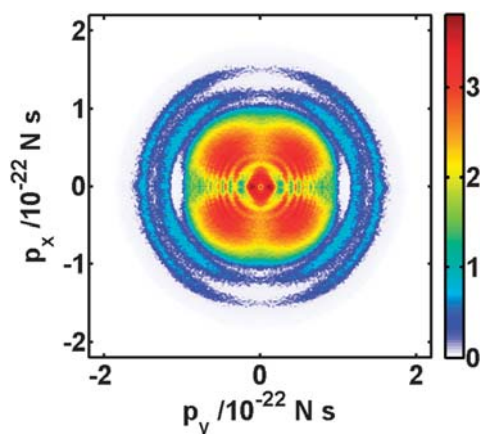


Fig. 8 Two-dimensional C^+ momentum image for CO dissociation in a 4 fs, $0.8 \times 10^{14} \text{ W cm}^{-2}$ laser field without phase stabilization. Reprinted from ref. 82 with copyright permission of Springer.

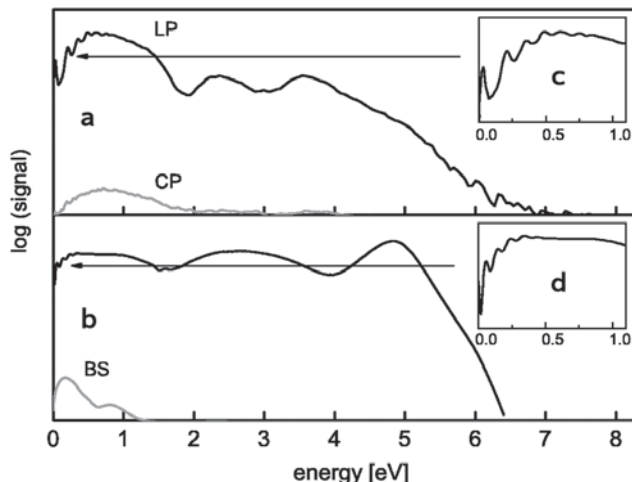


Fig. 9 (a) Experimentally observed C^+ kinetic energy spectra for CO dissociative ionization by linear (LP) and circular (CP) polarized light pulses without phase stabilization (integrated over 120°), (b) calculated C^+ kinetic energy spectrum including recollision excitation (RCE) and laser induced coupling of the bound and repulsive electronic states under the same conditions (bond softening; BS); the insets in (c) and (d) show the enlarged lower energy range for experimental and calculated spectra. Adapted from ref. 85 with copyright permission of Elsevier B.V.

find the C^+ yield to be approximately 20 times larger than the O^+ yield.

For CEP stabilized electric fields, there is a pronounced phase dependence on the directional ion emission for C^+ as well as for O^+ ions throughout the measured CEP range. The directional emission is represented according to eqn (15). $P_{\text{left}}(W, \phi)$ and $P_{\text{right}}(W, \phi)$ were obtained by integrating over an angular range of 120° around the polarization axis. Besides the kinetic energy spectrum (panel (a)) Fig. 10(b) displays the observed asymmetry $A(W, \phi)$ for the dissociative ionization of CO into C^+ and O as a function of the CEP and the kinetic energy W of the C^+ ion fragments. Fig. 10(c) shows the asymmetry parameter integrated over selected energy ranges (0.15–1.5 eV, 2–2.8 eV and 3.2–3.9 eV). The pronounced observed asymmetry in the directional emission of C^+ ions is almost equally strong throughout the whole kinetic energy spectrum. The CEP was calibrated by reference measurements in Xe and in comparison to calculations based on the quantitative rescattering theory.⁵¹ From the evaluation of these data we obtain an error in the absolute CEP of 0.04π . A similar asymmetry map (not shown here) was recorded for O^+ ions, showing the same features. However, due to the significantly weaker O^+ signal, the asymmetry map exhibits a significantly lower signal-to-noise ratio.

4.2.2 Theoretical interpretation of the dissociative ionization of CO with 740 nm pulses. In the presented experiment, the asymmetry can, in principle, arise from contributions of all three steps: ionization, recollisional excitation and laser-induced population transfer between excited electronic states of CO^+ during the dissociation (see Fig. 3). For the heteronuclear molecule, one can expect orientation-dependent ionization probabilities for phase stabilized lasers and thus a contribution from the ionization to the total observed asymmetry.^{43,46}

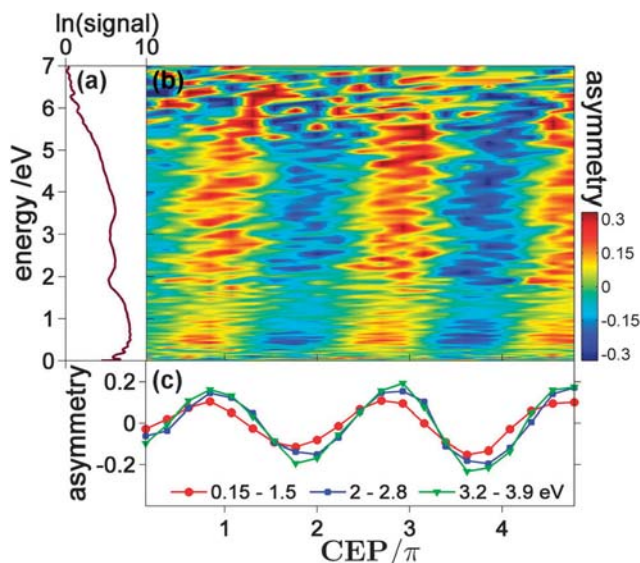


Fig. 10 (a) Measured C^+ kinetic energy spectrum for CO dissociative ionization. (b) Asymmetry of C^+ ion emission along the laser polarization (integrated over 120°) vs. kinetic energy and phase. (c) Asymmetry integrated over indicated energy ranges vs. CEP. Adapted from ref. 43.

Homonuclear diatomic molecules always show a symmetric angular distribution in the ionization step. For a detailed analysis of the asymmetry arising from the ionization step, see ref. 43. The contributions from the recollision are still unknown and their calculation is currently out of the scope for multi-electron molecules⁷⁸ such as CO.

In this part of the article we concentrate on the control of the electron motion during the dissociation of CO^+ . As pointed out in Section 4.2.1, the main part of the ionic fragments, which exhibit an asymmetry in the directional ion emission, is produced through recollision excitation. Thus we follow this pathway using theory to interpret the experimental results. For the multi-electron molecule CO^+ the choice of electronic states involved in the dissociation step is more demanding and guidance from the experiments is needed. The selection criteria are the energy distribution of the recolliding electron and the kinetic energy distribution of the ionic fragments (e.g. C^+ ions from the dissociation of CO^+ into $\text{C}^+ + \text{O}$). The first criterion defines an upper energy limit for the excited states involved in the dissociation. The cut off energy for the electron, which excites the parent ion under the present laser parameters is about 13 eV. This value corresponds to $3.17U_p$ where the ponderomotive potential U_p is given by:

$$U_p = \frac{e^2 E_0^2}{4m_e \omega^2}. \quad (19)$$

Therefore the PES for the CO electronic ground state, the first three $^2\Sigma$ states and the first six $^2\Pi$ states for the CO^+ molecular ion are calculated using the quantum chemistry package Molpro⁸³ on the CASSCF(6,12)/aug-cc-pVQZ and CASSCF(5,12)/aug-cc-pVQZ level of theory. These calculations include the highest lying σ and π electrons in the active space for the electron correlation. From the reachable excited state manifold we

chose three potential curves to represent the induced nuclear dynamics. An additional selection criterion was that all transitions among the selected states were allowed in order to steer the electronic motion efficiently. We included the $\text{C } ^2\Sigma^+$ state as the weakly bound state and the $\text{E } ^2\Pi$ state to mimic the repulsive dynamics. Both states correlate with the $\text{C}^+(^2\text{P}) + \text{O}(^1\text{D})$ channel. As the third PES, we include the $\text{H } ^2\Pi$ state, which is the first state leading to the $\text{C}(^3\text{P}) + \text{O}^+(^4\text{S})$ dissociation channel, delivering O^+ fragments as observed in the experiment. The CO electronic ground state, the CO^+ electronic ground state, the first $^2\Pi$ state and the three selected PES for the dissociation are depicted in Fig. 11. As the initial state for the dissociation after the RCE we assume a Gaussian energy distribution for the returning electron performing the excitation, and we start with a 55 : 38 : 7 linear combination of three selected states (ordered in increasing energy). This population distribution was proven to deliver the experimentally observed ratio between C^+ and O^+ fragments. Whether the initial population of the excited states (caused by the recollision) is slightly dependent on the CEP or not is an open question, but its calculation is currently beyond the scope for larger molecules.⁷⁸

For the quantum dynamical calculations, the CO^+ ions are taken to be aligned at an angle of 45° with respect to the laser polarization. This allows all transitions between the Σ and Π states. On the other hand the 45° orientation coincides with the angle for the maximum number of experimentally detected ionic fragments. Field-free rotation can be neglected in the calculations as it takes place on a much longer timescale (approximately 8.5 ps for a full rotation of CO at the equilibrium distance). Also dynamic alignment before dissociation induced by the laser field is neglected because of the extremely short pulse duration used in the experiments on CO (4 fs).⁹¹ The PES are represented on an equally spaced grid with 1200 points in the interval between 0.5 and 15 Å. As in Section 4.1.2, simulations start after the recollision, assuming ionization of CO only at the electric field maximum of the laser pulse and recollision of the electron after 1.7 fs.⁸⁶

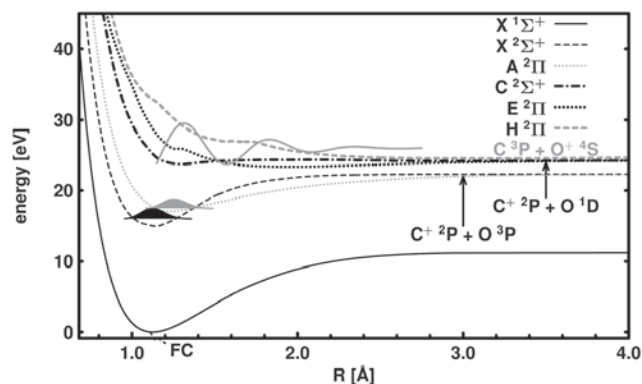


Fig. 11 PES of CO, CO^+ and the Franck-Condon (FC) point for the ionization from neutral CO obtained by calculations described in the text. Pathway for the formation of C^+ (O^+) ions from CO by dissociation of the molecular ion after recollision excitation. The remaining laser field (solid gray line) indicates coupling between the selected electronic states. Reprinted from ref. 85 with copyright permission of Elsevier B.V.

The kinetic energy spectrum for the C^+ ions derived from the nuclear dynamics is depicted in Fig. 9(b) and shows a reasonable qualitative agreement with the experimental data (Fig. 9(a)) supporting again the selection made for the representative states. On the basis of these results, we can explain the origin of the observed energy distribution. The low kinetic energy spectrum (0.15–1.5 eV) arises from the dynamics of the weakly bound $C^2\Sigma^+$ state. The spectrum in the range between 2.0 and 2.8 eV results from the purely repulsive $E^2\Pi$ state. Both states correlate with the $C^+ + O$ dissociation channel. The high energy spectrum reflects the dynamics of the second repulsive $H^2\Pi$ state correlating with the $C + O^+$ reaction channel. The structure in the low kinetic energy spectrum (see Fig. 9(d)) follows from interference effects in the nuclear wavepacket on the $C^2\Sigma^+$ state and can also be seen in the experimental spectrum. This interference appears as the recollision excitation produces a high energy wavepacket consisting of both bound and continuum vibrational states of the $C^2\Sigma^+$ PES. During the dissociation, the bound vibrational states are trapped in the potential well and interfere with the outgoing part of the wavepacket (see Fig. 12). The temporal evolution of the interference pattern can be directly connected to the vibrational levels of the $C^2\Sigma^+$ state.

We also included in the calculations the minor pathway of laser-induced excitation from low lying bound electronic states $X^2\Sigma^+$ and $A^2\Pi$ to the dissociative states of CO^+ which was predominantly observed in the experiments using CP light. Fig. 9(b) (BS) shows the resulting kinetic energy spectrum. Only small contributions are visible in the kinetic energy ranges 0.15–1.5 eV and 2.0–2.5 eV (the second contribution is not visible within the resolution of the figure).

The temporal evolution of the electric field and the electronic state population during the pulse interaction is shown in Fig. 13(a) and (b), respectively. The population dynamics reveal that only a weak coupling between the electronic states is achieved due to the laser interaction, because the conditions for a resonance between the selected electronic states are never fulfilled. By flipping the CEP by π , the temporal evolution of the population dynamics in the individual states is inverted.

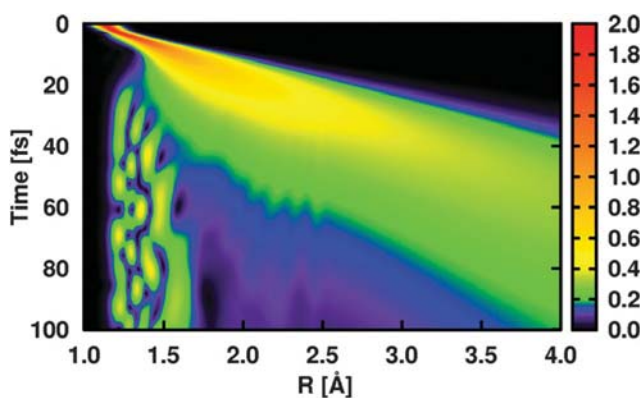


Fig. 12 Time evolution of the probability amplitude of the nuclear wavepacket in the $C^2\Sigma^+$ state of CO^+ as a function of the internuclear distance. Reprinted from ref. 85 with copyright permission of Elsevier B.V.

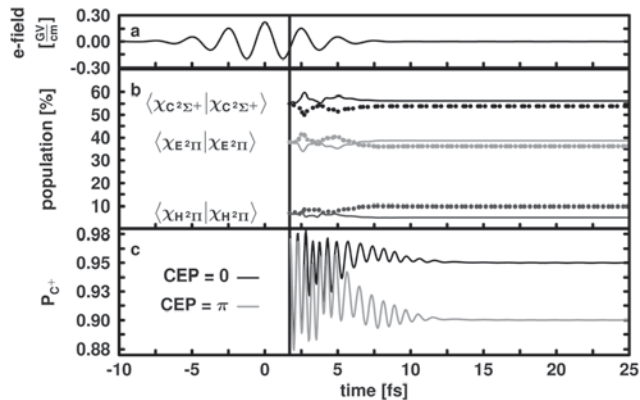


Fig. 13 Summary of the coupled electron- and nuclear dynamics during the dissociation. The black vertical line indicates the time of recollision, 1.7 fs after ionization at the maximum electric field. (a) Temporal evolution of the electric field. (b) Time-dependent populations of the $C^2\Sigma^+$, $E^2\Pi$ and $H^2\Pi$ states of CO^+ after recollision excitation (solid: CEP = 0; dotted: CEP = π). (c) Temporal evolution of the probability of measuring a C^+ fragment P_{C^+} for the dissociative ionization of CO^+ after recollision (black: CEP = 0; grey: CEP = π). Reprinted from ref. 43 with copyright permission of APS.

For the heteronuclear diatomic molecule CO , the definition of the asymmetry is slightly more complex compared to the calculations in Section 4.1.2. Here the experimentally measured asymmetry arises from the ensemble of randomly oriented CO molecules. Thus P_{left} and P_{right} have to be assigned to molecules with different orientations. From both orientations C^+ and O^+ fragments can be detected. Thus the asymmetry cannot be derived directly from the electron density of a single molecule with only one specific orientation. In the calculations we have direct access to the probability $P_{C^+}(t)$ of measuring a C^+ fragment for a given orientation. This probability is given by

$$P_{C^+}(t) = \int_{x_{min}}^{x_{max}} dx \int_{y_{min}}^{y_{max}} dy \int_{z_{min}}^0 dz \rho(r_1, t; R(t)) \quad (20)$$

where x , y and z refer to the molecular frame with z pointing along the intermolecular axis and the O-atom oriented along negative z -values. The CEP-dependent asymmetry as observed in the experiment can be calculated by the final $P_{C^+}(t)$ values from two different orientations.

The induced electron dynamics in an oriented CO^+ molecule, reflected in $P_{C^+}(t)$ (see Fig. 13(c)), occur again, but only until 6 fs, as a result of the competition between the influence of the light pulse, the dynamics of the linear combination and the interference term of the nuclear wavefunctions. As soon as the light induced population transfer between the electronic states stops (approximately after 8 fs, see Fig. 13(b)), the oscillation in $P_{C^+}(t)$ decreases rapidly, converging after 12 fs to its final value. During the dissociation, the MOs become localized on one of the two nuclei, converging to either the O- or C-atomic orbitals. Consequently, the value of the integral $\int \psi_{i,0}^*(r; R(t)) \psi_{j,0}(r; R(t)) dr_2 \dots dr_N$ (see eqn (8)) and thus the last term of eqn (8) vanishes. The damping of the oscillations in $P_{C^+}(t)$ reflects the decay of the initially prepared electronic coherence. When the dynamics of the electronic linear

combination is ceasing, the probability $P_{C^+}(t)$ upon the dissociation is given by the final population distribution of the coupled reaction channels leading either to C^+ or O^+ .⁸⁵ This ratio is steered very precisely by the CEP of ultrashort laser pulses. A shift of the CEP by π while keeping the molecular orientation leads to a different result (grey curve in Fig. 13(c)). Changing the orientation of the molecule by 180° is equal to shifting the CEP by π , as the transition dipole moment changes the sign. Thus in practice, the CEP-dependent asymmetry in the dissociation step can be calculated by $P_{C^+}(t)$ for two CEP values shifted by π . The maximum value for the resulting asymmetry due to the electron localization is around 0.03. This value is not directly comparable to the experimental values as the ionization has significant contributions to the total asymmetry. In contrast to homonuclear diatomic molecules, for heteronuclear diatomic molecules the ionization can dominate the total asymmetry.^{43,46} This was confirmed for CO by a recent study at higher intensity ($3.5 \times 10^{14} \text{ W cm}^{-2}$).³⁰

4.3 Enhancing the CEP control of electron localization by adapting the laser frequency

The experiments presented in Sections 4.1 and 4.2, are the first examples of sub-cycle charge-directed reactivity. The electron localization is controlled in both cases *via* the waveform of a few-cycle near-infrared laser pulse. Despite this enormous progress, a quantitative understanding of the achieved control over the electron dynamics in systems beyond the H_2^+ prototype is still very challenging. The nuclear- and electron-dynamics are strongly coupled and the overall dynamics involves several laser-driven processes which today cannot be easily treated all together within one approach. The dependence of the CEP-controlled electron localization on molecular hydrogen and its isotopologues has been explored as a function of laser parameters including intensity⁹² and pulse duration.⁴¹ Previous experiments and theory have indicated that CEP-control decreases exponentially with the number of laser cycles,^{41,61,64} making it necessary to keep the number of laser cycles for CEP-control small.

In order to achieve efficient laser-driven charge directed reactivity it is necessary to use pulses with durations matching the timescale of the nuclear dynamics. As an example, the dissociation time for the molecular hydrogen ion *via* bond-softening (BS)⁹³ may be estimated as *ca.* half of a vibrational period, corresponding to 12 fs.⁹⁴ In this sense, longer wavelengths produce electric fields with a significantly longer pulse duration than their counterparts in the NIR while the number of laser cycles is still small. Consequently, few-cycle laser pulses in the MIR regime are expected to result in efficient CEP control of reactions and can uncover new aspects of the strongly coupled laser-driven dynamics in molecules. In this part of the article we review our recent results on the sub-cycle control of the dissociative ionization of D_2 using intense few-cycle CEP-stable MIR (2.1 μm) laser fields.

4.3.1 Experimental results of the dissociative ionization of D_2 with 2.1 μm pulses. Few-cycle, CEP-stable MIR light pulses

with a center wavelength of 2.1 μm and a pulse duration of 25 fs were generated as detailed in Section 2.1. The laser pulses were focused to an intensity of $(6.2 \pm 1.5) \times 10^{13} \text{ W cm}^{-2}$ to dissociatively ionize D_2 . The resulting D^+ fragments were measured, as in the experiments described before, *via* VMI.³⁵ For pulses without phase stabilization, the cross section of the full 3D momentum distribution at $p_z = 0$ is very similar to Fig. 4 but reveals two more features. The most intense one is found in the spectral range between 0 and 1 eV and is assigned to BS. Three additional contributions can be identified at higher energies for the intervals 1–4 eV, 4–9 eV and 9–13 eV. The identification of these channels is discussed together with our theoretical calculations in Section 4.3.2.

The directional D^+ ion emission (as a function of the measured CEP and momentum p) is analyzed using the angle-integrated asymmetry parameter $A(p, \phi)$ (see eqn (15); the kinetic energy W is here replaced by the momentum p). The ion yields $P_{\text{left}}(W, \phi)$ and $P_{\text{right}}(W, \phi)$ were integrated over an opening angle of 20° along the laser polarization axis. The asymmetry $A(p, \phi)$ is shown in Fig. 14(a). A high degree of asymmetry with an amplitude of approximately 0.2 is found for energies below 1 eV, the energy range which corresponds to the BS channel. The asymmetry in this channel shows a slope in kinetic energy of its oscillation as a function of CEP with a phase jump at 0.17 eV. The observation of such a strong asymmetry in the BS channel is very remarkable when compared to earlier results obtained in the NIR.⁴² A second asymmetry contribution in the energy range 1–4 eV has a weaker (max. 0.1) amplitude and its oscillation with the CEP is independent of the momentum. A π phase-jump between the two channels is observed at *ca.* 1 eV. Above 4 eV only a vanishingly small asymmetry was measured under the experimental conditions.

4.3.2 Theoretical interpretation of the dissociative ionization of D_2 with 2.1 μm pulses. In the presented experiments

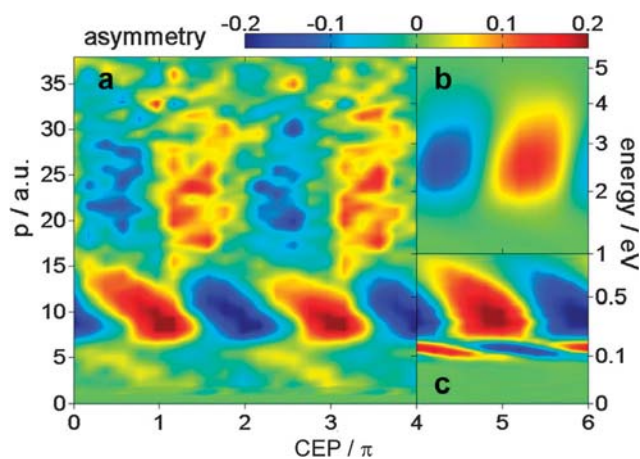


Fig. 14 (a) D^+ ion emission asymmetry as a function of the fragment momentum (corresponding kinetic energy scale on the right) and relative CEP of the D^+ ion emission obtained by integrating over a full opening angle of 20° along the laser polarization axis. (b) Asymmetry obtained by the calculations for the RCE channel. (c) Same as (b) for the BS channel. Adapted from ref. 70 with copyright permission of APS.

(Section 4.3.1), the bond softening pathway shows a distinct asymmetry in the ion ejection, which is even more pronounced than in the recollision-induced dissociation channel. Thus we include in our theoretical analyses, in contrast to the calculations in Sections 4.1 and 4.2, both pathways. To simulate the laser induced mechanism, we used the vibrational ground state wavefunction of the D_2 molecule to generate the initial wavepacket for the $X^2\Sigma_g^+$ potential. We further assumed that ionization takes place only at the peaks of the electric field, which corresponds to the highest ionization probability (schematically drawn in Fig. 15). In the case of the recollision-induced mechanism, the wavepacket is initially propagated on the $X^2\Sigma_g^+$ surface and projected either to the $A^2\Sigma_u^+$ surface (in the case of RCE) or to the D_2^{2+} surface (in the case of RCI (see Fig. 15)) at the time of recollision, which is $\frac{2}{3}$ of an optical cycle, *i.e.*, 4.7 fs at 2.1 μm .⁹⁵

The quantum dynamical calculations for the laser-induced dissociation mechanism including $X^2\Sigma_g^+$, $A^2\Sigma_u^+$ (and the 11 higher excited states) reproduced well the experimental spectrum below 2 eV.⁷⁰ Thus, this part of the spectrum is assigned to the BS channel. The contribution in the 4–9 eV energy range can be assigned to the direct population of the A-state during the ionizing half-cycle. This contribution is found to be an order of magnitude stronger in the MIR as compared to NIR excitation.⁷⁰ The high-energy tail of the measured D^+ spectrum (above 9 eV) is also captured by the calculations which include the 11 higher excited states. The spectrum resulting from a calculation for the RCE dissociation covers the energy range between 2 and 5 eV and explains the corresponding experimental signal. We also computed the spectrum resulting from RCI, which may occur due to the high ponderomotive potential in the MIR and thus high recollision energy (reaching up to 84.5 eV at $6.2 \times 10^{13} \text{ W cm}^{-2}$). Double ionization results in the Coulomb explosion of the involved molecule as well as the

production of two D^+ fragments that are emitted in opposite directions along the laser polarization axis. Thus, D^+ fragments from this dissociation channel cannot produce an asymmetry in the ion emission.

The calculated asymmetries corresponding to the dissociation of D_2^+ along the RCE and the BS pathway are shown in Fig. 14(b) and (c), respectively. In order to facilitate a quantitative comparison with the experimental data, the asymmetries were calculated assuming ionization at the 5 most intense extrema of the electric field. The two calculations were performed for the same absolute CEP. The asymmetry amplitude and its energy-dependent oscillatory behavior correlated to CEP are reproduced by the calculations.

The wavelength dependence of the asymmetry amplitude and the sign of the asymmetry are shown in Fig. 16. The asymmetry amplitudes for the BS channel considering ionization at the peak electric field (for $\phi = 0$) and using a 3.5-cycle pulse for different wavelengths are shown in Fig. 16(a). The asymmetry oscillates close to zero in the NIR regime, explaining the difficulty in observing the CEP-control in this channel with the 760 nm few-cycle pulses (see Section 4.1). By increasing the wavelength, the asymmetry amplitude increases. This behavior is now independent of the pulse duration.⁷⁰ The wavelength dependence of the RCE dissociation is shown in Fig. 16(b) as a function of the D^+ fragment kinetic energy and the recollision time. With increasing wavelength, the recollision time increases as well. This leads to population of the A-state at larger internuclear distances. As a result the kinetic energy of the D^+ fragments decreases, starting around 6 eV at 760 nm to less than 3 eV at 2.1 μm . As can be extracted from Fig. 16, the sign of the asymmetry in the two dissociation channels (*i.e.* BS and RCE) is strongly dependent on the wavelength. Therefore, the relative phase between the asymmetry oscillation of the two channels depends on the wavelength as well. Coincidentally, at

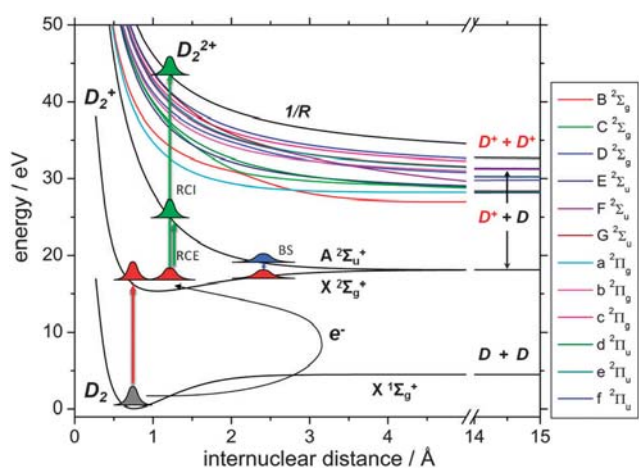


Fig. 15 Relevant potential energy surfaces of D_2 , D_2^+ and D_2^{2+} obtained by *ab initio* calculations. The higher lying excited electronic states of D_2^+ above the A-state are labeled alphabetically according to their symmetry. The red arrow indicates tunnel ionization of D_2 , the blue arrow indicates bond-softening (BS) and the green arrows indicate recollision induced excitation (RCE) and ionization (RCI). Reprinted from ref. 70 with copyright permission of APS.

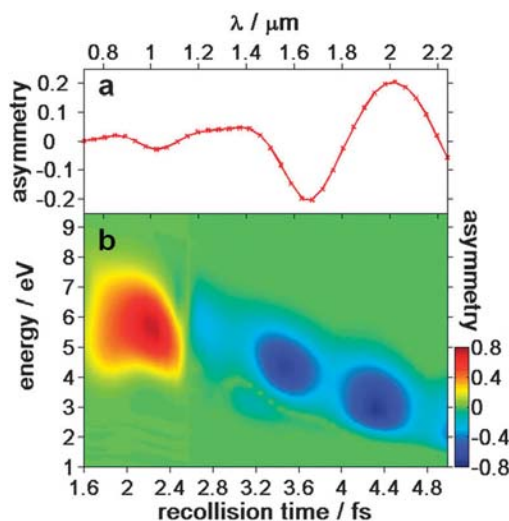


Fig. 16 (a) Asymmetry amplitude in the BS channel for various laser wavelengths assuming a 3.5-cycle pulse. (b) Asymmetry map as a function of kinetic energy and recollision time (corresponding to the wavelength given on the top axis). Reprinted from ref. 70 with copyright permission of APS.

2.1 μm the asymmetries of the two channels exhibit an opposite sign, reproducing the experimental observation.

4.4 Comparison of the mechanisms leading to electron localization

Although the experimental conditions discussed above have many similarities, a comparison of the observed mechanisms which lead to electron localization show three major differences. The first occurs already in the preparation step. In D_2^+ the superposition of the electronic states is created by the laser interaction. Thus the sign of the initial superposition depends directly on the CEP. Consequently, the electronic wavepackets prepared with opposite CEP values show exactly mirrored asymmetry values. In the case of CO^+ , the electron localization dynamics are triggered by recollision excitation. Thus the oscillation in $P_{\text{C}^+}(t)$ for different CEP values proceeds almost in phase initially and is altered later on. Here, the observed control arises from the interplay between the electronic wavepacket, prepared during the RCE, and the CEP of the applied electric field.

For the second difference, the electron localization in D_2^+ shows much larger amplitudes compared to CO^+ , because in this lighter molecule the nuclear dynamics are fast enough to hit the resonance with the laser frequency. The control is particularly efficient when the energy difference between the involved electronic states becomes comparable to the photon energy. In the case of the BS mechanism, the initially-prepared wavepacket moves towards the outer turning point of the ground state potential and gets coupled to the $\text{A } ^2\Sigma_u^+$ state at large internuclear distances (see Fig. 15). This mechanism is even more efficient for light pulses in the MIR regime, because here, the longer pulse duration matches the timescale of the induced nuclear dynamics with a small number of half cycles.

The third major difference is found in how the electron dynamics terminates. In the case of the D_2^+ molecule, the dynamics only stop when the two involved electronic states become degenerate and consequently the exponent in eqn (8) becomes zero. Simultaneously, the dissociation process is completed and the degree of electron localization is determined not only by the mixing ratio of the electronic states, but also by the final phase of the exponential factor. For the CO^+ molecule, the dynamics stop because the value of the integral $\int \psi_{i,0}^*(r; R(t)) \psi_{j,0}(r; R(t)) dr_2 \dots dr_N$ becomes zero when the MO localize on one atomic center and converge to the atomic orbitals. For internuclear distances around the minimum geometry the valence orbitals of both molecules are delocalized over both centers. By forming the linear combination, the electron density is in both cases localized on one atom. For larger internuclear distances the situation changes completely. In the case of homonuclear D_2^+ the two orbitals are still delocalized over the molecule and the linear combination still localizes the electron density. For heteronuclear CO^+ the molecular orbitals localize during the dissociation. Thus, the electron density of the superposition state is delocalized.

Consequently, the degree of electron localization is not determined by the phase evolution (second term of eqn (8)) but by the populations of the electronic states which localize the electron on one or the other nucleus in their asymptotic limits (e.g. C^+ or O^+ channels).

5 Control of D_2 dissociative ionization by a two-color femtosecond laser field

Controlling electron motion with waveforms shaped on a sub-cycle scale is feasible with CEP-controlled few-cycle pulses or waveform synthesized pulses. Recent experimental and theoretical examples for the application of simple two-color waveform synthesis in the femtosecond domain to control the dissociative ionization of molecular hydrogen demonstrate that in this case, longer laser pulses can be employed.⁹⁶ The asymmetric dissociation of D_2 can be tailored with the relative phase $\varphi_{\text{two-color}}$ of a two-color laser field $\varepsilon(t) = E_1(t) \cos(\omega t) + E_2(t) \cos(2\omega t + \varphi_{\text{two-color}})$ with frequencies ω and 2ω , respectively (e.g. corresponding to wavelengths of 800 nm and 400 nm).

Ray *et al.* have observed a very strong asymmetry in the emission of D^+ ions from D_2 (see Fig. 17), where relatively long, ca. 45 fs, linearly polarized pulses were employed.⁹⁶ The experimental results were further interpreted in terms of a model based on the dynamic coupling of the gerade and ungerade states in the D_2^+ molecular ion by the laser field.⁹⁶

The experiment shows the phase-dependent asymmetry *versus* the energy of the emitted ion (see Fig. 17). The asymmetries were associated with various dissociation channels including one-photon bond softening (BS), visible between 0 and 0.3 eV, two-photon above-threshold dissociation (ATD)⁹⁷ with a strong signal in the range of 0.3–2 eV and recollisional excitation (RCE). RCE results in an asymmetry at high energies above 3 eV. The strong signal centered near an ion energy of 3 eV corresponds to charge-resonance-enhanced-ionization (CREI)^{98,99} or enhanced ionization (EI), involving the double ionization of

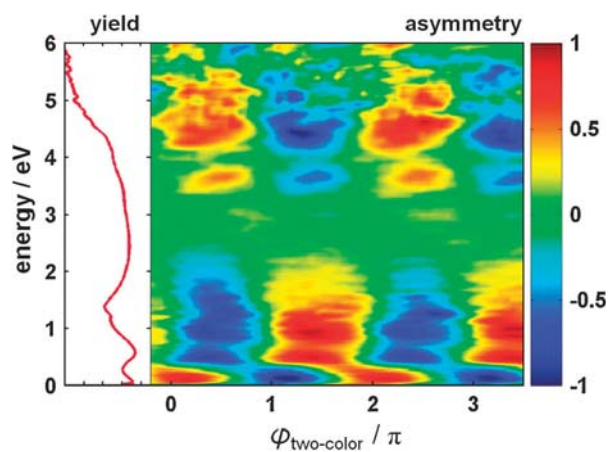


Fig. 17 Asymmetry of D^+ ion emission from D_2 as a function of ion energy and $\varphi_{\text{two-color}}$ being a phase between 800 nm and 400 nm pulses from ref. 96. The asymmetry is obtained using eqn (16) taking into account the number of ions integrated over an angle of 30° along the polarization axis. The ion spectrum (left panel) is shown on a logarithmic scale. Adapted from ref. 96.

D_2 and the generation of two deuteron ions and therefore no asymmetry, as is seen in Fig. 17.

6 Control of D_2 dissociative ionization by an attosecond EUV pump–femtosecond NIR probe scheme

Control of electron dynamics in molecular hydrogen can also be achieved using a pump–probe scheme: an attosecond extreme ultraviolet (EUV) pulse as the “pump” pulse and a weak, CEP-stabilized, few-cycle, NIR pulse as the “probe” pulse. Such a scheme was first implemented by Sansone *et al.*⁴⁷ where electron charge localization was observed in the dissociative ionization of H_2 and D_2 molecules. Isolated attosecond XUV pulses with a duration of 300–400 as extending from 20 to 40 eV¹² were generated through high-order harmonic generation (HHG) in krypton. The XUV pulses and time-delayed linear polarized IR pulses of 6 fs (FWHM) were crossed with an effusive H_2 or D_2 gas jet inside a VMI spectrometer⁵⁰ and the resulting H^+ or D^+ ions were detected. Fig. 18(a) shows measured kinetic energy distributions for D^+ fragments integrated over an angular range of 90° along the laser polarization direction

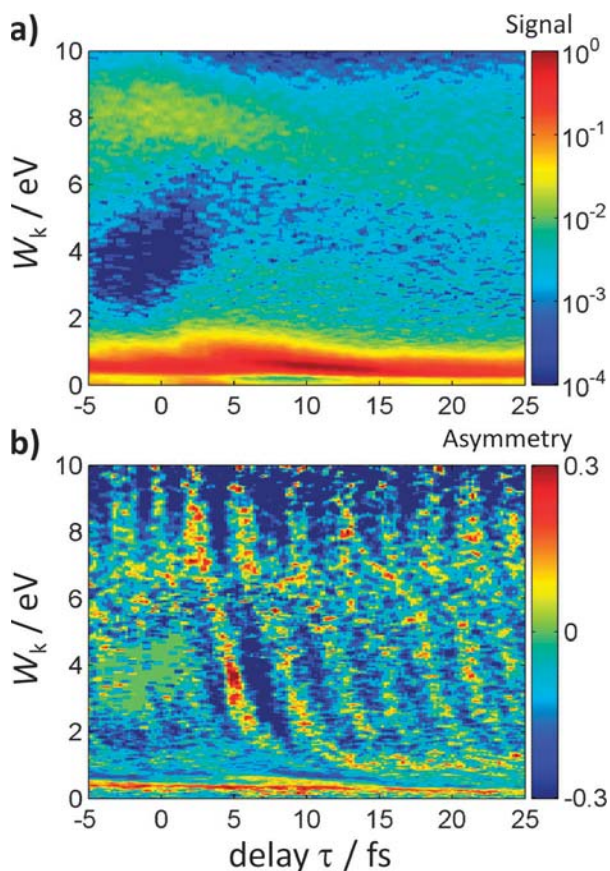


Fig. 18 Experimentally measured (a) kinetic energy distributions and (b) the asymmetry parameter for the formation of D^+ ions in two-color attosecond EUV-femtosecond NIR dissociative ionization of D_2 , as a function of the fragment kinetic energy W and the delay between the pump and probe pulses τ . Adapted from ref. 47.

as a function of the time delay τ . The dominating process at low kinetic energies ($W < 1$ eV) is the BS of the bound $X^2\Sigma_g^+$ state of D_2^+ caused by the NIR pulse. The signal attributed to the vibrational wavepacket peaks near $\tau \approx +11$ fs and is in good agreement with previous results on vibrational wavepacket motion in the D_2^+ ground state.⁹⁴ When the XUV and NIR pulses overlap ($\tau \approx 0$ fs), the D^+ signal strongly increases around 8 eV. The enhancement of the signal at high energies can be attributed to a growth in the excitation cross section of the $A^2\Sigma_u^+$ continuum state caused by infrared-laser-induced mixing of the $A^2\Sigma_u^+$ and $X^2\Sigma_g^+$ states. The increase may also contain contributions from photoionization of the $Q_1^1\Sigma_u^+$ doubly excited autoionizing states by the NIR laser. Fig. 18(b) shows the asymmetry of D^+ ion emission in opposite directions along the laser polarization vector. The time-dependent asymmetry parameter $A(W, \tau)$ exhibits pronounced oscillations as a function of the delay between the pump and probe pulses, τ .

The time-dependent asymmetry originates from two mechanisms, which are discussed briefly in the following. The first is similar to the already discussed mechanism on the CEP control of electron localization in D_2^+ , where the NIR field introduces the asymmetry through interaction with the dissociating molecule. The second mechanism involves the excitation of autoionizing states of the neutral D_2 . To allow conclusions on these mechanisms, Martín and coworkers have conducted quantum mechanical calculations, taking into account the $X^2\Sigma_g^+$ and $A^2\Sigma_u^+$ continua as well as the doubly excited states.¹⁰⁰ All electronic and vibronic (dissociative) degrees of freedom, electron correlations, and interferences between various ionization and dissociation paths were included. Important advantages of these calculations were that they not only achieved satisfactory agreement with experimental results,⁴⁷ but also allowed the analysis of the components of the two-electron wavefunctions, which are responsible for the asymmetry.

The main difference in the first mechanism as compared to the single-color CEP-control is that the EUV pulse leads directly to population of the $A^2\Sigma_u^+$ state. The propagating wavepacket is then coupled to the $X^2\Sigma_g^+$ state by the time-delayed NIR laser field. The asymmetry in this case depends on both the CEP of the NIR field and the delay between the EUV and the NIR pulse.

To understand the dissociation process in the second mechanism, it has to be considered *how* the coherent superposition leading to the final asymmetry was prepared. In this case the coherent superposition results from the direct population of the $A^2\Sigma_u^+$ state by the attosecond EUV pulse and the population of the $X^2\Sigma_g^+$ state through autoionization (see ref. 47 for details). A little bit more complex is the role of the NIR field in the second mechanism. The photoionization, which results in the population of the $A^2\Sigma_u^+$ state yields a photoelectron with angular momentum $l = 0$. A detailed analysis of the theoretical results for the temporal overlap of the EUV and NIR pulses and short delay times shows that the dominant contribution to the wavefunction that leads to an asymmetry consists of a coherent superposition of the $X^2\Sigma_g^+$ and $A^2\Sigma_u^+$ states with formation of an electron with $l = 1$.⁴⁷

The NIR field therefore does not interact with the molecular ion but with the freed electron. This is a fascinating result as it indicates that the action of the NIR field on the freed electron determines the localization of the second electron.

The experiment with EUV pump and NIR probe pulses indicates a much better control over electron dynamics, which can be exploited for the control of the dynamics in more complex molecules. For dissociation reactions, the temporal delay between the two pulses can be adjusted to the dissociation time.

7 CEP reaction control mediated by conical intersections

On the basis of the knowledge gained in the sections above, we designed a scheme for the control of a photochemical reaction by guidance of an electronic wavepacket. It is well known that many ultrafast photo-induced reactions proceed *via* conical intersections (CoIns).^{102,103} These important regions on the potential energy surface can serve as “points of no return” for nuclear dynamics, deciding through which pathway the reaction proceeds. Due to non-adiabatic coupling, population is transferred between the intersecting electronic states. Here, a superposition and hence an electronic wavepacket can be formed or projected back to one eigenstate. In addition, the time scales of the electron and nuclear dynamics are well synchronized in the vicinity of CoIns. Here, the energy difference between the coupled electronic states becomes very small, slowing the dynamics of the (usually much faster) electrons to the timescale of the nuclear dynamics. Directly at the intersection point, the energy gap goes to zero and the electron dynamics stop, comparable to the dissociation of the D_2^+ molecule discussed see Section 4.1. In the vicinity of a CoIn, the electron and nuclear motion are strongly coupled, as here, the nuclei have time to react to the slowly varying electronic potential. Hence, a molecular reaction should be sensitive to the control of the phase of an electronic wavepacket near a CoIn.

Following the experiments presented in Section 6 we utilize a high energy pump pulse and a CEP stabilized MIR control pulse. The first one is needed to start the photochemical reaction by transferring population from the electronic ground state S_0 to an electronically excited state, for example S_2 . The system then evolves from S_2 towards the CoIn between S_2 and a second excited state, *e.g.* S_1 . Just before the coupling region is reached, the phase stable IR pulse prepares a superposition between the electronic states S_1 and S_2 , just as in the D_2^+ experiments. Again, this prepared superposition gives rise to an electronic wavepacket, whose phase is imprinted by the CEP of the MIR control field. In contrast to the experiments involving dissociation, where the phase of the superposition causes asymmetric ion ejections, the electronic wavepacket propagates through the CoIn and the imprinted phase translates into a distinct population ratio between the involved electronic states.

In order to demonstrate the efficiency of this scheme we constructed a two dimensional model system. In accordance with ref. 104 we constructed three 2D potential energy surfaces

(H_{00} , H_{11} and H_{22}) on the diabatic basis using the internal coordinates R_1 and R_2 . These potentials give rise to a diabatic coupling (H_{12}) between the upper two electronic states. Along the R_1 coordinate we used three different Morse potentials, describing the main reaction coordinate driving the system towards the CoIn. The R_2 direction is represented by different harmonic potentials, characterized by their respective force constants. Motion along this coordinate lifts the degeneracy away from the CoIn. The complete parameter set including the masses (M_{R_1} and M_{R_2}) is given in ref. 101. To use the adiabatic approach, which was described in Section 3.3, we transformed the model system from the diabatic basis into the adiabatic basis by diagonalizing the Hamiltonian matrix including the diabatic coupling.¹⁰⁵ This leads to the potential energy surfaces S_0 , S_1 and S_2 as well as the corresponding mixing angle θ between the diabatic states. The adiabatic states exhibit a non-adiabatic coupling between S_1 and S_2 at $R_1 \simeq 3.81 \text{ \AA}$, $R_2 = 0$. A one dimensional cross section of the surfaces S_0 , S_1 and S_2 at $R_2 = 0$ is shown in Fig. 19(a), together with a two dimensional representation around the CoIn in the inset. The corresponding NACs $f_{12}^{(R_1)}$ and $f_{12}^{(R_2)}$ (already including the masses) are shown in Fig. 19(b) and (c).

Incorporating these NACs into our nuclear wavepacket propagation (see Section 3.3) allows us to monitor the dynamics including the non-adiabatic population transfer between the upper electronic states. Due to the non-adiabatic coupling between the electronic states, the electron dynamics is already included implicitly. All calculations start in the electronic and vibrational ground states.

As a reference, we first only investigated the dynamics induced by the pump pulse. For the high energy pulse, we used a sub-10-fs (here: 3 fs FWHM) Gaussian pulse, resonant to the S_0 - S_2 transition (190 nm) with a moderate maximum electric field of 100 GV cm^{-2} . A short and resonant pump pulse is needed to produce a narrow and well localized wavepacket on the excited state, which later can be efficiently coupled to the S_1 state. During the first 10 fs, the pump pulse transfers 26% from the S_0 (Fig. 20(a), solid black line) to the S_2 state (Fig. 20(a), dashed gray line). Then the system evolves freely towards the CoIn, which is reached approximately 35 fs after the start of the propagation. This becomes visible in the population exchange between S_2 and S_1 (Fig. 20(a), dashed dotted gray line). After the complete wavepacket has passed the coupling region (after approximately 50 fs) both excited states are almost evenly populated (see Fig. 20(a)). For the full control scheme we added the MIR control pulse (3.0 \mu m , 12 fs FWHM, 100 GV cm^{-2} , CEP = 0.1π) with a delay to the first pulse of 40 fs. The resulting population dynamics, also shown in Fig. 20(a), exhibits major differences. As attempted, the second pulse transfers population from S_2 (dashed black line) to S_1 (dashed dotted black line) and prepares the electronic wavepacket. When the nuclear wavepacket reaches the coupling region (around 35 fs), nearly equal populations in both excited states are reached by the control pulse. Afterwards, during the non-adiabatic coupling (between 35 and 50 fs) the prepared superposition leads to 19% population in the S_2 and only 7% in the S_1 state.

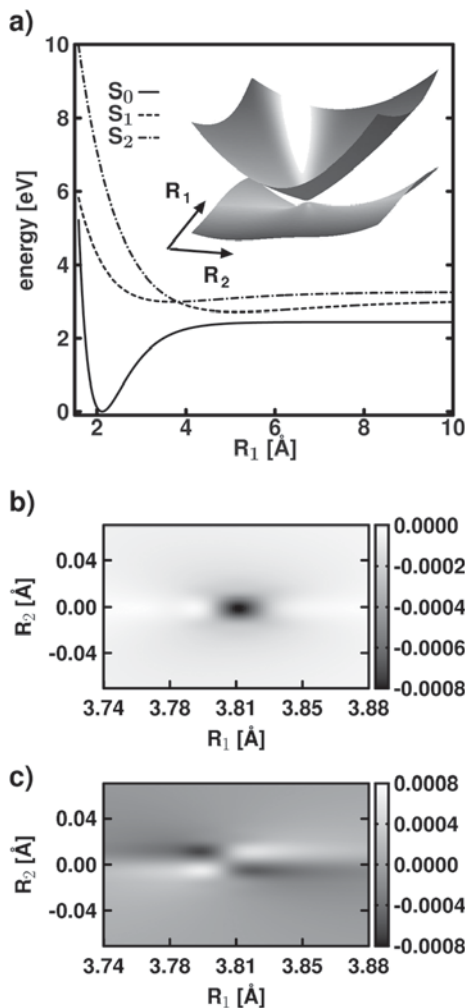


Fig. 19 (a) 1D cross section of the 2D adiabatic potential energy surfaces S_0 , S_1 and S_2 at $R_2 = 0$. Inset: 2D representation of the adiabatic potential energy surfaces S_1 and S_2 in the vicinity of the Con. NAC elements $J_{12}^{(R_1)}$ (b) and $J_{12}^{(R_2)}$ (c) already including the masses. Adapted from ref. 101.

Changing the CEP of the MIR control pulse from 0.1π (Fig. 20(b)) to 0.6π (Fig. 20(c)) and 1.1π (Fig. 20(d)), *i.e.* changing the phase of the prepared electronic wavepacket, reveals major changes in the population dynamics and shows the control mechanism. The control pulse for each case is plotted in the insets (solid black line) together with a reference pulse (CEP = 0; solid gray line). During the first 35 fs we observe the same dynamics in the three cases Fig. 20(b–d). The pump pulse populates the S_2 state (dashed black line) within the first 10 fs. Then, the control MIR pulse builds up the S_2 – S_1 (dashed dotted black line) superposition state between 20 and 35 fs. The differences in these dynamics occur as soon as non-adiabatic coupling becomes dominant. For a CEP of 0.1π (Fig. 20(b)) the superposition prepared by the MIR-field results in a final population ratio of 7 : 19 ($\approx 24 : 76$ normalized to the population initially transferred to the S_2 state). In Fig. 20(c), where CEP = 0.6π , a final population ratio of 13 : 13 ($\approx 50 : 50$ normalized to the population initially transferred to the S_2 state) is achieved. For a CEP value of 1.1π (Fig. 20(d))

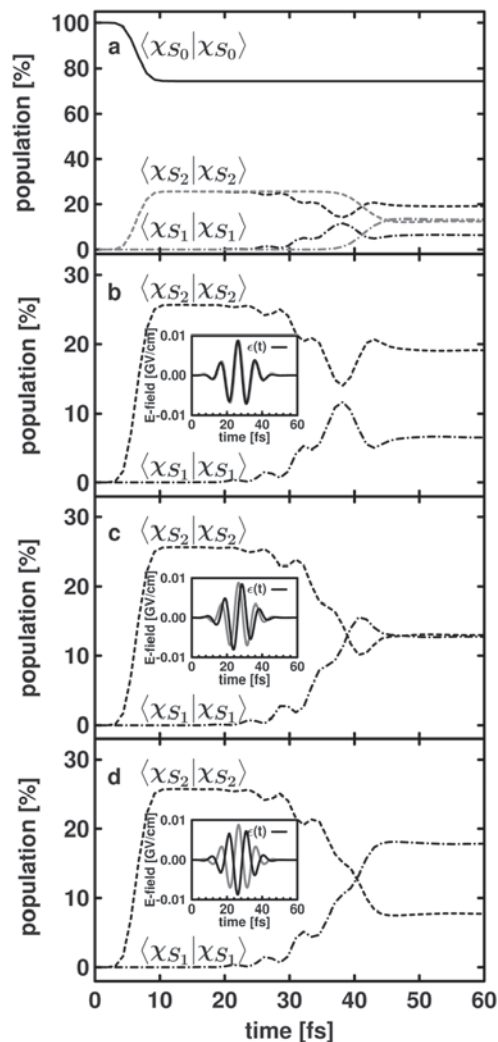


Fig. 20 (a) Population dynamics of the proposed model system including only the pump (solid black, dashed gray and dashed dotted gray line) and including the pump and control pulse (solid black, dashed black and dashed dotted black line). (b–d) Temporal evolutions of the populations in the S_1 (dashed black line) and S_2 states (dashed dotted black line), for the CEP values 0.1π (b), 0.6π (c), and 1.1π (d). The three population dynamics show very different behavior during the non-adiabatic coupling (between 35 and 50 fs) due to the different phases of the prepared wavepacket imprinted by the CEP of the MIR control field. The used control pulses are shown in the insets (solid black line) together with the reference pulse with a CEP equal to zero (solid gray line). Reprinted from ref. 101 with copyright permission of IEEE.

the final population ratio of 18 : 8 ($\approx 74 : 26$ normalized to the population initially transferred to the S_2 state) is nearly the inverted result to that obtained for a CEP of 0.1π (Fig. 20(b)), reflecting the phase shift of π in the electric fields for both cases.

Fig. 21 shows the final populations in the target states (S_1 : dashed dotted black line; S_2 : dashed black line) as a function of the CEP of the MIR control pulse. Within the used pulse parameters, we found it is possible to steer the final population ratio $S_1 : S_2$ within the boundaries of 7 : 19 and 18 : 8 very precisely by changing the CEP of the MIR pulse. The loss in control efficiency (maximum boundaries of 26 : 0 and 0 : 26) can

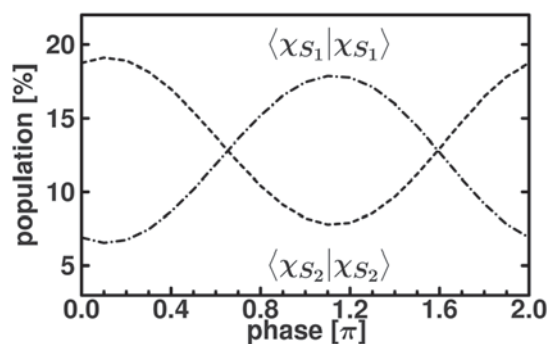


Fig. 21 Final populations of the S_1 (dashed line) and the S_2 (dashed dotted line) as a function of the carrier envelope phase of the MIR control pulse. The population initially transferred to the S_2 state is 26%. Reprinted from ref. 101 with copyright permission of IEEE.

be assigned to the imperfect preparation of the superposition by the MIR control pulse.

The observed control can be understood as follows: changing the CEP changes the phase of the prepared superposition, *i.e.* the phase of the electronic wavepacket. The NAC elements imprint a constant phase on the superposition state. Thus, the interplay between both phases now defines the path through the CoIn and simultaneously the final branching ratio. As a consequence, the CEP is a highly efficient knob, which is capable of controlling such a photoreaction very precisely.

8 Conclusions

Attosecond science is coming of age and is presently reaching a level of maturity and sophistication that allows the detailed investigations of the role of multi-electron dynamics in physics and chemistry.^{32,106} Coherent control of electron motion in molecules may be achieved *via* steering electrons with the electric field of light. Tailoring oscillatory fields by the carrier-envelope phase has already permitted a great degree of control over the outcome of simple chemical reactions. In the future, we will likely see a much higher degree of control with the use of synthesized waveforms which may be sculpted with sub-cycle precision, going beyond oscillatory waves.^{10,32}

Strong coupling between electron and nuclear motion gives access to the control of even heavier particles, and strong-field driven electron dynamics provides a knob to control more complex chemical reactions. The first results in this direction have been achieved recently with the control of the ionization and dissociation of hydrocarbons.⁴⁸ The current development of high-repetition rate (hundreds of kHz), amplified few-cycle laser systems permitting the generation of (isolated) attosecond light pulses is expected to greatly aid the progress of the research by allowing researchers to perform attosecond coincidence measurements. Along with the development of these experimental techniques that we expect to mature over the next years, the interpretation of the experiments will largely benefit from continued efforts of theory development to treat more complex molecules and chemical reactions in the presence of strong laser fields.

Acknowledgements

We acknowledge the many contributions of our co-workers and close collaborators to the research results presented in this article and Brady Steffl for support in editing the manuscript. We are grateful for support from the Max-Planck Society and the DFG *via* grants Kl-1439/2, Kl-1439/3, Kl-1439/5 and the Cluster of Excellence: Munich Center for Advanced Photonics (MAP). M.F.K. acknowledges partial personal support from the US Department of Energy under grant DE-FG02-86ER13491 and the NSF under grant NSF-PHY11-25915.

References

- 1 A. H. Zewail, *J. Phys. Chem. A*, 2000, **104**, 5660–5694.
- 2 B. J. Sussman, D. Townsend, M. Y. Ivanov and A. Stolow, *Science*, 2006, **314**, 278–281.
- 3 J. Breidbach and L. S. Cederbaum, *Phys. Rev. Lett.*, 2005, **94**, 033901.
- 4 H. Hennig, J. Breidbach and L. S. Cederbaum, *J. Phys. Chem. A*, 2005, **109**, 409–414.
- 5 F. Remacle and R. D. Levine, *Proc. Natl. Acad. Sci. U. S. A.*, 2006, **103**, 6793.
- 6 R. Weinkauf, P. Schanen, D. Yang, S. Soukara and E. W. Schlag, *J. Phys. Chem.*, 1995, **99**, 11255–11265.
- 7 A. Baltuška, *et al.*, *Nature*, 2003, **421**, 611.
- 8 T. Wittmann, *et al.*, *Nat. Phys.*, 2009, **5**, 357–362.
- 9 T. Rathje, *et al.*, *J. Phys. B: At., Mol. Opt. Phys.*, 2012, **45**, 074003.
- 10 A. Wirth, *et al.*, *Science*, 2011, **334**, 195–200.
- 11 M. Schultze, *et al.*, *J. Electron Spectrosc. Relat. Phenom.*, 2011, **184**, 68.
- 12 G. Sansone, *et al.*, *Science*, 2006, **314**, 443.
- 13 N. G. Johnson, *et al.*, *Phys. Rev. A: At., Mol., Opt. Phys.*, 2011, **83**, 013412.
- 14 F. Süßmann, *et al.*, *Rev. Sci. Instrum.*, 2011, **82**, 093109.
- 15 X. Gu, *et al.*, *Opt. Express*, 2009, **17**, 62.
- 16 I. Ahmad, *et al.*, *Appl. Phys. B: Lasers Opt.*, 2009, **97**, 529.
- 17 I. Ahmad, *et al.*, *New J. Phys.*, 2011, **13**, 093005.
- 18 L. Gallmann, *et al.*, *Appl. Phys. B: Lasers Opt.*, 2000, **70**, S67–S75.
- 19 P. Bates, O. Chalus and J. Biegert, *Opt. Lett.*, 2010, **35**, 1377–1379.
- 20 J. Itatani, *et al.*, *Phys. Rev. Lett.*, 2002, **88**, 173903.
- 21 R. Kienberger, *et al.*, *Nature*, 2004, **427**, 817.
- 22 D. Jones, *et al.*, *Science*, 2000, **288**, 635–639.
- 23 R. Holzwarth, *et al.*, *Phys. Rev. Lett.*, 2000, **85**, 2264–2267.
- 24 A. Apolonski, *et al.*, *Phys. Rev. Lett.*, 2000, **85**, 740.
- 25 A. J. Verhoef, *et al.*, *Opt. Lett.*, 2006, **31**, 3520.
- 26 S. Koke, *et al.*, *Nat. Photonics*, 2010, **4**, 462.
- 27 F. Lücking, *et al.*, *Opt. Lett.*, 2012, **37**, 2076–2078.
- 28 M. Kübel, *et al.*, *New J. Phys.*, 2012, **14**, 093027.
- 29 B. Bergues, *et al.*, *Nat. Commun.*, 2012, **3**, 813.
- 30 K. J. Betsch, *et al.*, *Phys. Rev. A: At., Mol., Opt. Phys.*, 2012, **86**, 063403.
- 31 E. Goulielmakis, *et al.*, *Nature*, 2010, **466**, 739.
- 32 F. Krausz and M. Y. Ivanov, *Rev. Mod. Phys.*, 2009, **81**, 163.

- 33 G. Cerullo, A. Baltuška, O. Mücke and C. Vozzi, *Laser Photonics Rev.*, 2011, **5**, 323–351.
- 34 B. Bergues, *et al.*, *New J. Phys.*, 2011, **13**, 063010.
- 35 A. T. J. B. Eppink and D. H. Parker, *Rev. Sci. Instrum.*, 1997, **68**, 3477.
- 36 J. Ullrich, *et al.*, *Rep. Prog. Phys.*, 2003, **66**, 1463.
- 37 M. F. Kling, *et al.*, *New J. Phys.*, 2008, **10**, 025024.
- 38 X. Liu, *et al.*, *Phys. Rev. Lett.*, 2004, **93**, 263001.
- 39 J. Mauritsson, *et al.*, *Phys. Rev. Lett.*, 2010, **105**, 053001.
- 40 M. F. Kling, *et al.*, *Science*, 2006, **312**, 246–248.
- 41 M. F. Kling, *et al.*, *Mol. Phys.*, 2008, **106**, 455.
- 42 M. Kremer, *et al.*, *Phys. Rev. Lett.*, 2009, **103**, 213003.
- 43 I. Znakovskaya, *et al.*, *Phys. Rev. Lett.*, 2009, **103**, 103002.
- 44 Y. Liu, *et al.*, *Phys. Rev. Lett.*, 2011, **106**, 073004.
- 45 B. Fischer, *et al.*, *Phys. Rev. Lett.*, 2010, **105**, 223001.
- 46 I. Znakovskaya, *et al.*, *Phys. Chem. Chem. Phys.*, 2011, **13**, 8653.
- 47 G. Sansone, *et al.*, *Nature*, 2010, **465**, 763.
- 48 X. Xie, *et al.*, *Phys. Rev. Lett.*, 2012, **109**, 243001.
- 49 S. Zherebtsov, *et al.*, *Nat. Phys.*, 2011, **7**, 656.
- 50 O. Ghafur, *et al.*, *Rev. Sci. Instrum.*, 2009, **80**, 033110.
- 51 S. Micheau, Z. Chen, A. T. Le, J. Rauschenberger, M. F. Kling and C. D. Lin, *Phys. Rev. Lett.*, 2009, **102**, 073001.
- 52 M. J. J. Vrakking, *Rev. Sci. Instrum.*, 2001, **72**, 4084–4213.
- 53 K. C. Kulander, *Phys. Rev. A: At., Mol., Opt. Phys.*, 1987, **36**, 2726–2738.
- 54 E. Runge and E. K. U. Gross, *Phys. Rev. Lett.*, 1984, **52**, 997.
- 55 T. Klamroth, *Phys. Rev. B: Condens. Matter Mater. Phys.*, 2003, **68**, 245421.
- 56 N. Rohringer, A. Gordon and R. Santra, *Phys. Rev. A: At., Mol., Opt. Phys.*, 2006, **74**, 043420.
- 57 T. Kato and H. Kono, *Chem. Phys. Lett.*, 2004, **392**, 533.
- 58 J. Zanghellini, M. Kitzler, T. Brabec and A. Scrinzi, *J. Phys. B: At., Mol. Opt. Phys.*, 2004, **37**, 763.
- 59 A. I. Kuleff, J. Breidbach and L. S. Cederbaum, *J. Chem. Phys.*, 2005, **123**, 044111.
- 60 A. D. Bandrauk, S. Chelkowski and H. S. Nguyen, *Int. J. Quantum Chem.*, 2004, **100**, 834–844.
- 61 V. Roudnev and B. D. Esry, *Phys. Rev. Lett.*, 2007, **99**, 220406.
- 62 M. Nest, *Chem. Phys. Lett.*, 2009, **472**, 171–174.
- 63 K. Yagi and K. Takatsuka, *J. Chem. Phys.*, 2005, **123**, 224103.
- 64 D. Geppert, P. von den Hoff and R. de Vivie-Riedle, *J. Phys. B: At., Mol. Opt. Phys.*, 2008, **41**, 074006.
- 65 C. Leforestier, *et al.*, *J. Comput. Phys.*, 1991, **94**, 59–80.
- 66 A. Hofmann and R. de Vivie-Riedle, *Chem. Phys. Lett.*, 2001, **346**, 299–304.
- 67 W. Domcke and G. Stock, *Adv. Chem. Phys.*, 1997, **100**, 1–169.
- 68 J. Voll, T. Kerscher, D. Geppert and R. de Vivie-Riedle, *J. Photochem. Photobiol., A*, 2007, **190**, 352.
- 69 T. Brixner and G. Gerber, *ChemPhysChem*, 2003, **4**, 418–438.
- 70 I. Znakovskaya, *et al.*, *Phys. Rev. Lett.*, 2012, **108**, 063002.
- 71 V. Roudnev, *et al.*, *Phys. Rev. Lett.*, 2004, **93**, 163601.
- 72 S. Chelkowski, T. Zuo, O. Atabek and A. D. Bandrauk, *Phys. Rev. A: At., Mol., Opt. Phys.*, 1995, **52**, 2977–2983.
- 73 S. Chelkowski, M. Zamojski and A. D. Bandrauk, *Phys. Rev. A: At., Mol., Opt. Phys.*, 2001, **63**, 023409.
- 74 J. Levesque, S. Chelkowski and A. D. Bandrauk, *J. Mod. Opt.*, 2003, **50**, 497.
- 75 X. M. Tong, S. Watahiki, K. Hino and N. Toshima, *Phys. Rev. Lett.*, 2007, **99**, 093001.
- 76 F. He, C. Ruiz and A. Becker, *Phys. Rev. Lett.*, 2007, **99**, 083002.
- 77 D. S. Murphy, J. McKenna, C. R. Calvert, I. D. Williams and J. F. McCann, *New J. Chem.*, 2007, **9**, 260.
- 78 S. Graefe and M. Y. Ivanov, *Phys. Rev. Lett.*, 2007, **99**, 163603.
- 79 A. S. Alnaser, *et al.*, *Phys. Rev. Lett.*, 2003, **91**, 163002.
- 80 A. S. Alnaser, *et al.*, *Phys. Rev. Lett.*, 2004, **93**, 183202.
- 81 H. Sakai, *et al.*, *Phys. Rev. A: At., Mol., Opt. Phys.*, 2003, **67**, 063404.
- 82 P. von den Hoff, *et al.*, *Appl. Phys. B: Lasers Opt.*, 2010, **98**, 659.
- 83 H.-J. Werner, *et al.*, *MOLPRO, version 2006.1*, a package of *ab initio* programs, 2006, see <http://www.molpro.net>.
- 84 R. Franke, *Math. Comput.*, 1982, **38**, 181–200.
- 85 P. von den Hoff, I. Znakovskaya, M. F. Kling and R. de Vivie-Riedle, *Chem. Phys.*, 2009, **366**, 139.
- 86 H. Niikura, F. Légaré, R. Hasbani, A. D. Bandrauk, M. Y. Ivanov, D. M. Villeneuve and P. B. Corkum, *Nature*, 2002, **417**, 917.
- 87 A. S. Alnaser, *et al.*, *Phys. Rev. A: At., Mol., Opt. Phys.*, 2005, **71**, 031403.
- 88 B. K. McFarland, J. P. Farrell, P. H. Bucksbaum and M. Gühr, *Science*, 2008, **322**, 1232.
- 89 H. Akagi, *et al.*, *Science*, 2009, **325**, 1364–1367.
- 90 O. Smirnova, *et al.*, *Nature*, 2009, **460**, 972–977.
- 91 X. M. Tong, *et al.*, *J. Phys. B: At., Mol. Opt. Phys.*, 2005, **38**, 333.
- 92 F. He, A. Becker and U. Thumm, *Phys. Rev. Lett.*, 2008, **101**, 213002.
- 93 P. H. Bucksbaum, *et al.*, *Phys. Rev. Lett.*, 1990, **64**, 1883–1886.
- 94 T. Ergler, *et al.*, *Phys. Rev. Lett.*, 2006, **97**, 193001.
- 95 J. Hu, M.-S. Wang, K.-L. Han and G.-Z. He, *Phys. Rev. A: At., Mol., Opt. Phys.*, 2006, **74**, 063417.
- 96 D. Ray, *et al.*, *Phys. Rev. Lett.*, 2009, **103**, 223201.
- 97 A. Zavriyev, *et al.*, *Phys. Rev. A: At., Mol., Opt. Phys.*, 1990, **42**, 5500.
- 98 T. Zuo and A. D. Bandrauk, *Phys. Rev. A: At., Mol., Opt. Phys.*, 1995, **52**, R2511–R2514.
- 99 A. D. Bandrauk, *Comments At. Mol. Phys. D*, 1999, **1**(3), 97.
- 100 J. L. Sanz-Vicario, H. Bachau and F. Martín, *Phys. Rev. A: At., Mol., Opt. Phys.*, 2006, **73**, 033410.
- 101 P. von den Hoff, R. Siemering, M. Kowalewski and R. de Vivie-Riedle, *IEEE J. Sel. Top. Quantum Electron.*, 2012, **18**, 119–129.
- 102 M. Klessinger, *Angew. Chem.*, 1995, **107**, 597–599.
- 103 *Conical Intersections. Electronic Structure, Dynamics & Spectroscopy*, ed. W. Domcke, D. R. Yarkony and H. Köppel, World Scientific, 2004, vol. 15.
- 104 P. Cattaneo and M. Persico, *J. Phys. Chem. A*, 1997, **101**, 3454–3460.
- 105 D. Simah, B. Hartke and H.-J. Werner, *J. Chem. Phys.*, 1999, **111**, 4523.
- 106 M. F. Kling and M. J. J. Vrakking, *Annu. Rev. Phys. Chem.*, 2008, **59**, 463–492.